

Key features of the IPSL ocean atmosphere model and its sensitivity to atmospheric resolution

O. Marti, P. Braconnot, J.-L. Dufresne, J. Bellier, R. Benshila, S. Bony, P. Brockmann, P. Cadule, A. Caubel, F. Codron, N. de Noblet, S. Denvil, L. Fairhead, T. Fichefet, 5 M.-A. Foujols, P. Friedlingstein, H. Goosse, J.-Y. Grandpeix, E. Guilyardi, F. Hourdin, A. Idelkadi, M. Kageyama, G. Krinner, C. Lévy, G. Madec, J. Mignot, I. Musat, D. Swingedouw, and C. Talandier

Climete Dynamics, accepted 23/07/2009

CLIDY-D-08-00104

10 1 Abstract

This paper presents the major characteristics of the Institut Pierre Simon Laplace (IPSL) coupled ocean-atmosphere general circulation model. The model components and the coupling methodology are described, as well as the main characteristics of the climatology and interannual variability. The model results of the standard version used for IPCC climate projections, 15 and for intercomparison projects like the Paleoclimate Modeling Intercomparison Project (PMIP 2) are compared to those with a higher resolution in the atmosphere. A focus on the North Atlantic and on the tropics is used to address the impact of the atmosphere resolution on processes and feedbacks. In the North Atlantic, the resolution change leads to an improved representation of the storm-tracks and the North Atlantic Oscillation. The better representa- 20 tion of the wind structure increases the northward salt transports, the deep-water formation and the Atlantic meridional overturning circulation. In the tropics, the ocean-atmosphere dynamical coupling, or Bjerknes feedback, improves with the resolution. The amplitude of ENSO (El Niño-Southern oscillation) consequently increases, as the damping processes are left unchanged.

25 2 Keywords

Climate ; simulations ; ocean ; atmosphere; coupling; circulation; El Niño/Southern oscillation ; North-Atlantic oscillation; storm-tracks; resolution; coupling.

3 Affiliations

30 O.Marti (✉) • P. Braconnot • P. Friedlingstein • J. Bellier • P. Brockmann • A. Caubel • N. de Noblet
IPSL/LSCE, unité mixte CEA-CNRS-UVSQ,
Bât 712, Orme-des-Merisiers, F91191 Gif-sur-Yvette Cedex, France
E-mail : olivier.marti@lsce.ipsl.fr

35 J.-L. Dufresne • F. Hourdin • F. Codron • S. Bony • L. Fairhead • J.-Y. Grandpeix • I. Musat
IPSL/LMD, Unité mixte CNRS-Ecole Polytechnique-ENS-UPCM, case 99, 4 place Jussieu, F75252 Paris Cedex 05, France

D. Swingedouw
CNRS/CERFACS, 42 Avenue Gaspard Coriolis, F31057 Toulouse, France

- 40 H. Goosse • T. Fichefet
Institut d'Astronomie et de Géophysique Georges Lemaître,
Université Catholique de Louvain, Chemin du Cyclotron, 2, 1348, Louvain-la-Neuve, Belgium
- 45 J. Mignot • E. Guilyardi • R. Benshila • C. Lévy • G. Madec • C. Talandier
IPLS/LOCEAN, unité mixte CNRS-IRD-UPMC, case 100, 4 place Jussieu, F75252 Paris Cedex 05, France
- S. Denvil • P. Cadule • M.-A. Foujols
Institut Pierre Simon Laplace des Sciences de l'Environnement (IPSL), 4 place Jussieu, F75252 Paris Cedex 05, France
- 50 G. Krinner
LGGE, Unité mixte CNRS-UJF Grenoble, BP96, 38402 Saint-Martin-d'Hères, France

4 Introduction

55 Climate is the result of complex interactions between several subsystems. To understand how climate evolves depending on external forcing, climate system models are becoming more and more complex. Starting from atmosphere only models in the 60s', climate models incorporate now components of ocean, sea ice, land, vegetation, and possibly the carbon cycle, the atmospheric chemistry, atmospheric aerosols or oceanic tracers. These powerful tools are commonly used for future climate projections (IPCC 2007, Fig. 4b).

60 The IPSL CM4 model (Marti et al. 2005) couples four components of the Earth system: LMDZ (Hourdin et al. 2006) for atmospheric dynamics and physics, OPA (Madec et al. 1997) for ocean dynamics, LIM (Fichefet and Morales-Maqueda 1997; 1999) for sea ice dynamics and thermodynamics, and ORCHIDEE (Krinner et al. 2005) for the land surface. Successive versions of the global coupled model have been developed since 1995. Since the first version
65 of the coupled model, our goal was to design and develop a global coupled model with no flux correction at the air sea interface that can be used to study present, future and past climates. Substantial development and analysis concerned the conservation of energy and water, so that comprehensive analyses of heat and water budget and transport are possible.

The first version of the model (Braconnot et al. 1997) was built with the LMD5.3 version of
70 the LMD atmospheric model, the OPA 7 version of the ocean model developed at LODYC, and a simple sea ice component. The first coupled simulations (Braconnot et al. 1997) exhibited a large drift in surface air temperature, which has been attributed to an energetic imbalance of the atmospheric model. Several adjustments were performed. A first set of modifications has improved the atmosphere boundary layer over mixed sea ice and ocean grid
75 cells. A second set was designed to equilibrate the atmospheric model, by adjusting the threshold for vertical diffusion in stable cases, which allowed for better simulation of temperature inversions at high latitudes (Krinner et al. 1997). Other adjustments concern the drag coefficient in stable cases and the balance between long wave and short wave radiation at the top of the atmosphere (reduction of the water droplet size from 15 μm to 8 μm).
80 Although these adjustments allow stable coupled simulations, the energy absorbed in the tropical region was underestimated, which explains the cold tropical bias in the tropics (Braconnot et al. 2000). Mid-latitude experienced a reversed bias. These characteristics improved with a new version of the Morcrette et al. (1986) radiative scheme. The hydrological cycle was also closed in this revised version, thanks to a simple routing scheme
85 that considered the 46 major rivers (Le Clainche 1996). Following the work of Guilyardi et al. (2001), isopycnal diffusion was implemented in the ocean model. A revised version of the interpolation scheme (Marti et al. 2005) also contributed to the local and global conservation of energy at the air-sea interface.

The next step of the model development consisted in implementing the complex IPSL
90 thermodynamic sea ice model (L'Heveder 1999; Filiberti et al. 2001). This required some adjustment in the coupling procedure. In particular, in this IPSL CM2 version, the sea ice model computed sea ice albedo, and other surface parameters (Braconnot et al. 2000). The derivative of the fluxes with respect to temperature was also provided to the sea ice model to insure the stability of the coupling over sea ice, following the detailed stability analysis of
95 Dufresne et al. (1996). This version of the model yields to interesting results about the analyses of the response of the climate to changes in insolation (Braconnot and Marti 2003; Khodri et al. 2005). It was also coupled to a carbon cycle model, to perform the first climate simulations (present and future) with an interactive carbon cycle (Friedlingstein et al. 2001; Dufresne et al. 2002). However, some biases in the model climatology needed to be corrected.
100 Increased interest for mid and high latitudes climate leads also to the need for a better

resolution at high latitudes. Due to the cold bias of the model in the tropics, several aspects of the tropical interannual variability, such as the representation of ENSO (El Niño-Southern Oscillation), needed improvement.

105 The latest developments lead to a completely new model used for CMIP3 (Meehl et al. 2007), the multimodel ensembles climate projections used in the Intergovernmental Panel on Climate Change (IPCC) assessment report AR4 (IPCC 2007). The model climatology and the representation of the interannual variability were greatly improved compared to the previous generations, even though some biases are still present. The objective of this paper is to present the major characteristics of the IPCC AR4 version of the coupled model (Dufresne et al. 110 2005) and of its climatology. The results of the reference version are now in several databases (and PMIP II Braconnot et al. 2007; CMIP, Meehl et al. 2007), and used in several scientific works. This paper aims to help the database users by explaining the main characteristics of the simulated climate, and the origin of the model biases. Several aspects of model climatology and variability are affected by the resolution. From the reference version at 115 medium resolution, we discuss the impact of the atmospheric resolution on the key climatic features in the tropics and the mid-latitude.

Section 2 of the paper presents the model components and the methodology of the coupling. Section 3 presents the experiments, their global energetics, and the main characteristics of the surface climate. Section 4 focuses on two regions, Atlantic and tropics, and discusses the 120 mechanisms yielding to differences between the two resolutions. Conclusion is given in section 5.

5 The model

5.1 Model components

5.1.1 The atmospheric model LMDZ

125 The atmospheric component of the IPSL CM4 model, LMDZ (Hourdin et al. 2006), is a state-of-the-art atmospheric general circulation model, inherited from the original climate model of Laboratoire de Météorologie Dynamique of Sadourny and Laval (1984).

The dynamical part of the code is based on a finite-difference formulation of the primitive equations of meteorology. The discretization insures numerical conservation of both 130 enstrophy for barotropic flows and angular momentum for the axi-symmetric component. Vapor and liquid water are advected with a monotonic second order finite volume scheme (Van Leer 1977; Hourdin et al. 1999). For the current grids the time-step is of 2 hours for the radiation scheme, 30 minutes for physics, and 6 minutes (standard resolution) or 3 minutes (high resolution) for the dynamics. For latitudes poleward of 60° in both hemispheres, a 135 longitudinal filter is applied in order to limit the effective resolution to that at 60°.

Coupled to the dynamical core, the model includes a set of physical parameterizations. The radiation scheme is the one introduced several years ago in the model of European Centre for Medium-Range Weather Forecasts (*ECMWF*) by Morcrette (1986): the solar part is a refined version of the scheme developed by Fouquart and Bonnel (1980) and the thermal infra-red 140 part is due to Morcrette et al. (1986). Condensation is parameterized separately for convective and non-convective clouds. Moist convection is treated using mass flux approaches. During the preparation of the IPSL CM4 model, Emanuel (1991) convection scheme was adopted in place of Tiedtke (1989) scheme. The sensitivity of the simulated climate to the convection scheme has been studied by Hourdin et al. (2006) for the atmosphere alone, and by Braconnot et al. (2007) for the ocean-atmosphere model. Clouds are represented through a log-normal 145 probability distribution function of subgrid scale total (vapor and condensed) water (Le Treut

and Li 1991; Bony and Emanuel 2001). Effects of mountains (drag, lifting, gravity waves) are accounted for using a state-of-the-art scheme (Lott 1997; 1999).

150 For coupling purposes, a fractional land-sea mask was introduced in the model. Each grid box was then divided into four sub-surfaces corresponding to land surface, free ocean, sea ice and glaciers. Surface fluxes are computed using parameters (roughness length, albedo, temperature, humidity etc...) adapted to each surface type. For each atmospheric column, vertical diffusion is applied independently for each sub-surface, and the resulting tendencies are averaged. In addition an interface model was also introduced to disconnect more easily surface
155 processes from the atmosphere (see section 5.2). The diffusion scheme was rewritten to systematically force the boundary layer by surface fluxes. The computation of surface fluxes is done in an independent model that requires providing this model with the sensitivity of the turbulent flux to temperature, in order to preserve the properties of the semi-implicit scheme. With this formulation the flux model can be either a routine in the atmospheric model, an
160 ocean model or a land surface scheme.

5.1.2 The land surface model ORCHIDEE

ORCHIDEE (Krinner et al. 2005) is divided in three modules, devoted respectively to hydrology, carbon cycle and vegetation dynamics. Only the hydrological module SECHIBA (Ducoudré et al. 1993; Verant et al. 2004) is activated here. It has been developed as a set of
165 surface parameterizations for an atmospheric general circulation model. It describes the short-timescale processes (of the order of a few minutes to hours) of energy and water exchanges between the atmosphere and the biosphere. The parameterizations of photosynthesis follow Farquhar (1980) for C₃ plants and Collatz (1992) for C₄ plants. Stomatal conductance is calculated following Ball (1987), including the dependence on CO₂ concentration. The other two
170 modules have not been activated in this study.

ORCHIDEE includes (in SECHIBA) a routing scheme which combines the horizontal flow of water in the river basins with the vertical processes classically included in land-surface models. It is based on the work of Hagemann and Dümenil (1998), and uses a cascade of
175 three reservoirs: the stream and two aquifer reservoirs, each being associated with only one time constant. In each grid-cell the runoff and drainage are the water supply of the routing system. ORCHIDEE in this configuration has been validated over a wide range of regions and time scales and gives satisfactory results as discussed in Verant et al. (2004) and Ngo-Duc et al. (2005). The description of land ice included in ORCHIDEE is not used when coupled to the atmosphere.

180 5.1.3 The oceanic component: the OPA System

The OPA system (Andrich 1988; Madec et al. 1997) is a primitive equation model of both the regional and global ocean circulation. The OPA reference manual (Madec et al. 1997) details the ocean physics as taken into account by the model (explicitly or using sub-grid parameterization) as well as boundary conditions (surface, bottom, lateral), numerical schemes and computer implementation (<http://www.lodyc.jussieu.fr/opa>).
185

The ocean configuration used here is named ORCA2. Its specificity lies on the horizontal curvilinear mesh used to overcome the North Pole singularity found for geographical meshes. The common geographical coordinate system has a singular point at the North Pole that cannot be easily treated in a global model without filtering. A solution consists in the use of a
190 tripolar grid (Madec and Imbard 1996; Murray 1996). The grid is based on a 2° Mercator mesh (i.e. variation of meridian scale factor as cosine of the latitude). In the northern hemisphere the mesh has two poles, over Canada and Siberia. The ratio of anisotropy is nearly one everywhere. The mean grid spacing is about 2/3°. The latitudinal resolution is refined to 1° near the equator, and in the Mediterranean Sea. The Gibraltar Strait is explicitly

195 resolved, with a width of 111 km. The vertical domain spreads from the surface to a depth of 5000 m. There are 31 levels, with 10 levels in the top 100 m.

The eddy viscosity coefficient on momentum depends on the geographical position. It is taken as $40,000 \text{ m}^2 \text{ s}^{-1}$, reduced to $2,000 \text{ m}^2 \text{ s}^{-1}$ in the equator regions except near the western boundaries. Diffusion on tracer acts along the isopycnal surfaces (neutral surfaces) with an eddy diffusivity coefficient of $2,000 \text{ m}^2 \text{ s}^{-1}$. The eddy induced velocity parametrization uses a coefficient that depends on the growth rate of baroclinic instabilities (it usually varies from $15 \text{ m}^2 \text{ s}^{-1}$ to $3,000 \text{ m}^2 \text{ s}^{-1}$). The Beckman (1998) diffusive bottom boundary layer parameterization is applied along continental slopes. A linear friction is applied on momentum. To parameterize ocean convection, the vertical eddy viscosity and diffusivity coefficients are increased to $100 \text{ m}^2 \text{ s}^{-1}$ in case of static instability. The free surface formulation of Roullet and Madec (2000) is used.

5.1.4 The LIM sea ice model

LIM (Louvain-la-Neuve sea Ice Model) is a thermodynamic-dynamic sea ice model specifically designed for climate studies (Fichefet and Morales-Maqueda 1997; 1999). Sensible heat storage and vertical heat conduction within snow and ice are determined by a three-layer model (one layer for snow and two layers for ice). The effect of the subgrid-scale snow and ice thickness distributions is accounted for through an effective thermal conductivity, which is computed by assuming that the snow and ice thicknesses are uniformly distributed between zero and twice their mean value over the ice-covered portion of the grid cell. The storage of latent heat inside the ice resulting from the trapping of shortwave radiation by brine pockets is taken into account. The surface albedo is parameterized as a function of the surface temperature and the snow and ice thicknesses. The model allows for the presence of leads within the ice pack. Vertical and lateral growth and decay rates of the ice are obtained from prognostic energy budgets at both the bottom and surface boundaries of the snow-ice cover and in leads. Snow aging is parameterized identically in LIM, ORCHIDEE and LMDZ. The viscous-plastic constitutive law proposed by Hibler (1979) is used for computing the internal ice force. The ice strength is taken as a function of the ice thickness and compactness. The sea ice model runs on the same grid as OPA.

5.2 The coupled model

5.2.1 Coupling between atmosphere and surface

The coupling scheme of the previous versions of the IPSL model (Braconnot et al. 2000; Dufresne et al. 2002) has been revisited to ensure both global and local conservations of momentum, heat and fresh water fluxes at the air-sea interface. Following some of the ideas implemented in previous model versions (Dufresne and Grandpeix 1996; Braconnot 1998), an interface model was implemented in the atmospheric model. Each atmospheric column is interfaced with up to four different surface types: ocean, land, sea ice and land ice. Turbulent surface fluxes and surface temperature are computed separately on each subsurface, according to the surface characteristics (roughness length, stability etc. ...). The fluxes are sent to each sub-model (ocean, sea ice, land, glacier). In the atmosphere, the flux is the weighted sum of the fluxes computed for each subsurface. The computation of turbulent fluxes is detailed in the appendices. The radiative fluxes are computed in the atmospheric column, and redistributed on each subsurface taking into account the local properties of each subsurface (*i.e.* the albedo for the short wave flux, and temperature for the long wave flux). The redistribution is conservative. The coupling sequence yields a small loss or gain in energy and water. The LMDZ model computes average surface fluxes over free ocean and over sea ice during the coupling time step $t-1$ (currently one day). These fluxes are then sent to ORCA that uses them with a sea ice cover that has evolved, and keeps evolving during the time step t . At the end of

time-step t , the integrated flux received by the ocean could thus be slightly different from those sent at the end of time-step $t-1$.

245 5.2.2 Atmosphere / Ocean / Sea ice coupling

Fig. 1 shows the fields exchanged between ocean, atmosphere and sea ice. For most of the fields, the sea ice model acts as an interface model between atmosphere and ocean. The sea ice model receives the fluxes for free ocean and sea ice. It computes the evolution of sea ice, and computes the fluxes at the interface between the sea-ice and the ocean. The ocean receives only average fluxes and does not know the fraction of sea-ice. The ocean-sea ice interaction is exactly the same when the ocean-ice model is forced by climatology (e.g. see Timmermann et al. 2004) or coupled to an atmosphere model.

250 Amongst the fields sent by the atmosphere is $\partial Q/\partial T$. This field is the derivative of turbulent heat fluxes over sea ice with respect to surface temperature. To compute the temperature at the upper surface of the ice, LIM uses an implicit scheme for which the derivative of non-solar fluxes is needed. LIM computes the derivative of the long wave flux using the black body law, and adds the part from turbulent fluxes computed by LMDZ. The OASIS coupler (Valcke 2006) is used to synchronize the models, and interpolate and exchange fields.

5.2.3 Grids, interpolations and coastline.

260 The atmosphere (LMDZ) and the surface model (ORCHIDEE) run on a regular longitude/latitude grid whereas the ocean (OPA) and sea ice (LIM) run on a stretched grid. Vector fields (wind stress) are interpolated from atmosphere to ocean with a bicubic scheme. Scalar fields (heat and water fluxes, temperatures, sea ice fractions and albedos, but not calving) are interpolated using a first-order conservative remapping (Jones 1999).

265 The ocean bathymetry and coastline are derived from the 2-minute resolution Etopo2 bathymetry file of NGDC (National Geophysical Data Center), which is a combination of the satellite-based bathymetry (Smith and Sandwell 1997) and IBCAO in the Arctic (Jakobsson et al. 2000). It has been merged with the BEDMAP data (Lythe and Vaughan 2001) beyond 72°S in the Antarctic. In the ocean, a grid box is either fully ocean ($mask=1$) or fully land ($mask=0$). To keep exactly the same coastline in the ocean and the atmosphere models, the ocean mask is interpolated toward the atmosphere using the method used for scalar fields. This gives the fractions of land and ocean in each atmospheric grid box. In the ocean fraction, repartition between free ocean and sea-ice is given by the sea-ice model at each coupling step. The atmosphere computes the fluxes on each subsurface, allowing an exact local and global conservation of each quantity, even at the coast.

5.2.4 Closure of the fresh water budget

280 Snow can accumulate on some grid points, particularly on glaciers. The effect will be a decreased of the sea level. In nature, and if the climate is stable, the dynamics of the ice-sheet should compensate the sea level depletion, through the calving of iceberg. Calving needs to be taken into account in the water budget. On land-ice surface, the local snow mass is limited to 3,000 kg m⁻². At each time-step, the snow mass over this limit is sent as calving to the ocean, with a time filtering over ten years (see annex 9.3). A specific interpolation scheme is applied to calving: Earth is divided in three latitude bands with limits at 90°S/50°S/40°N/90°N. In each band, the calving is integrated and evenly sent to the ocean in the same latitude band. As the model is used for paleoclimate studies (Braconnot et al. 1999; Kageyama et al. 1999; Pinot et al. 1999; Kageyama et al. 2001; Alkama et al. 2006), the 40°N limit was chosen because it corresponds to the southernmost latitude reached by icebergs during ice ages (Heinrich events). For the northern band, the calving is sent to the Atlantic and

the Arctic, but not to the Pacific. Calving pours directly in the ocean, under sea ice, like river run-off.

In the ocean model several 'seas' are separated from the global ocean (North American Great Lakes, Caspian Sea and Black Sea). The global balance of water is equilibrated in the model. When averaged over the ocean and over several decades, the water flux going into the ocean (net result of precipitation, run-off, calving and evaporation) is close to zero. This is not true for each individual closed area, which may create a net transfer of water between the global ocean and the closed sea. To avoid any drift of salinity in both closed seas and global ocean, closed seas benefit from a special treatment. The water budget over each individual closed sea is set to zero. The water that should pour into each closed sea (or evaporates from) is added to the water budget of the global ocean, with three different schemes: (i) for the Black Sea, the water budget of the closed sea goes to closest oceanic grid point, mimicking the water flux in the straits; (ii) for the North American Great Lakes, if the water budget is positive (excess of water), it goes to the ocean, at the mouth of the St-Lawrence river. If it is negative (evaporation), it is spreaded over the whole open ocean; (iii) for the Caspian sea, the water budget, either positive or negative, is spreaded over the whole open ocean.

6 Experiments and main characteristics

6.1 Experiments

Two simulations are presented in the paper, that use the same ocean model and two different atmospheric resolutions. Experiment CTRL is run with a horizontal resolution of the atmosphere of 96 points in longitude and 71 points in latitude ($3.7^\circ \times 2.5^\circ$). This model corresponds to the reference version of the IPSL model used for future climate projection (Dufresne et al. 2005) for the IPCC AR4 report. The HiRes experiment uses a 144×96 atmospheric resolution ($2.5^\circ \times 1.875^\circ$). Both simulations use 19 levels on the vertical, and the same set of model parameters in all submodels, with no change of turbulent viscosity and diffusion. Before coupling, the atmosphere model is equilibrated so that the net heat flux at the top of the atmosphere is close to zero in global and multi-year averages (absolute value less than $0.1 \text{ W}^{-1} \text{ m}^{-2}$) under modern condition. The tuning only affects the radiative properties of the atmosphere. It concerns parameters such as the droplet size or the subgrid scale distribution of water vapour following Hourdin et al. (2006). Then the model is coupled. The simulations considered use present concentrations of greenhouse gases (**Table 1**). In HiRes, the same model parameters are used. No specific tuning was needed to equilibrate the surface flux. A larger resolution change would probably implies a specific parameter tuning.

For CTRL, the initial state of the ocean is rest, with temperature and salinity set to the values of the Levitus (1982) atlas at January 1st. Initial state of atmosphere is a January 1st of the ERA15 reanalysis from ECMWF (<http://www.ecmwf.int/research/era/ERA-15>). The soil model starts with a water content of 300 mm, and no snow cover. HiRes branches off CTRL at year 213, using the ocean and sea ice states of CTRL. Atmosphere, soil and snow over land and land ice restart from the same initial states as the one used for CTRL. Both simulations end at year 500. The mean state and the mean seasonal cycle of years 401 to 500 are used for all diagnoses.

6.2 Model adjustment

CTRL exhibits three main phases of adjustment (**Fig. 2**). First, fluxes at top of atmosphere (TOA) and at surface adjust rapidly, in about two years, and so does surface temperature. During this period, about half of the final snow cover is built. During the next 20 years, the snow cover and the sea ice continue to accumulate to reach almost their final state. Ocean topmost layers (the top 100 m) stabilize within the same time frame. The final stabilization

period lasts about 150 years, corresponding to a slow decrease of the ocean transport in the Atlantic, and to an increase of the snow cover in the Northern Hemisphere. Sea-ice increases (not shown), with a strong inter-annual variability. The upper 600 m of the ocean stabilizes during this period. After this adjustment, the model drift becomes negligible, with a global heat budget of -0.15 W m^{-2} at the surface. The global ocean temperature drift is $0.5^\circ\text{C}/\text{millennium}$.

HiRes branches from CTRL with a spun-up ocean and sea ice, but with no snow cover. The stabilization of HiRes also shows three phases, with similar time scales as for CTRL. The snow cover builds up rapidly, but with a reduced extend compared to CTRL (**Fig. 2**). Surface variables (temperature, albedos, ...) stabilize within a few years from 90°S to 30°N , which explains why the surface budget adjusts very rapidly (**Fig. 2**). From 30°N to 90°N , the adjustment of temperature, snow cover and sea-ice is slower, and takes about 100 years in the Arctic. HiRes stabilizes with a warmer globally averaged temperature (by 0.87°C) than CTRL (**Table 2**). The drift of temperature and salinity in the deep ocean (below 1000m) are detailed in **Table 3**. They are lower than $0.6^\circ\text{C}/\text{millennium}$ and $0.1 \text{ PSU}/\text{millennium}$ for both experiments in all basins.

The difference in the adjustment of HiRes and CTRL is driven by differences in surface albedo induced by reduced snow and sea-ice cover in HiRes over most of the continental regions in the northern Hemisphere and in the high latitudes (**Fig. 3**). These surface changes over the continent are mainly due to differences in the large-scale atmospheric circulation. Along 40°S the differences seen in **Fig. 3** correspond to a southward shift of the major pattern of the circulation and are discussed in section 7.3. The differences in albedo and temperature are consistent with more solar radiation entering the system in HiRes (3.18 W m^{-2}) and more infrared radiation emitted to space (3.24 W m^{-2}). The difference in clear sky solar radiation at the surface between the two experiments (2.61 W/m^2) is similar to the clear sky change in short wave (SW) at the top of the atmosphere (TOA), and represents most of the change in SW radiation. The absorption of the atmospheric column and the cloud radiative forcing have thus only a limited contribution to the SW radiative change, suggesting that the changes in solar radiation are driven by surface conditions, and mostly snow and sea-ice. The excess solar energy in HiRes is balanced at the surface by increased evaporation (3.02 W m^{-2}). The other surface heat fluxes do not change significantly between the two experiments. Changes in the atmospheric temperature profile and the water content both contribute to increase the greenhouse effect of the atmosphere by 1.82 W/m^2 , which also feedback on the temperature adjustment. Here the green house effect is simply estimated by the difference between the surface emission and the long wave heat flux at TOA. It is not possible from our rough estimates to separate the different effects on the longwave radiation.

The difference in the snow cover and the longwave feedback drives most of the difference in the short term adjustment between HiRes and CTRL (**Fig. 2**). Then the longer time scale (100 yrs) needed to reach a surface equilibrium in albedo and temperature corresponds to the time needed in HiRes to reduce the sea-ice cover in high latitudes. It is associated to an increase of the ocean heat transport in the Atlantic (see below).

6.3 Final state

The differences in surface adjustment between the two simulations also affect part of the atmosphere and ocean column. For the atmospheric part of the system, the major differences between the coupled model and observations follow the patterns seen in atmosphere alone simulations (Hourdin et al. 2006). The zonal mean of temperature exhibits a cold bias of about 8°C at 200 hPa in CTRL (**Fig. 4**). This pattern was attributed to an overestimation of the moisture content at this level in the LMD model, amplified by the coupling with the ocean (Braconnot et al. 2007). There is a systematic shift of the atmospheric structures (jet stream,

385 temperature) toward the equator already seen in atmosphere only simulations (Hourdin et al.
2006). This yields cold mid-latitudes in the atmosphere and the upper ocean in both ex-
periments. In the southern subtropics and high latitudes, the signal penetrates down in the
ocean. At other latitudes, the vertical gradient of oceanic temperatures is not steep enough in
390 the model, with too cold surface temperature (except near the equator), and an ocean too
warm in the upper 1000 m. However, the differences do not exceed 1°C in most places. The
salinity is too low north of 30°N in CTRL by about 1.5 PSU at the surface. This surface bias
extends to about 500, with gradual decrease. This bias has been attributed to the southward
shift of the major pattern of the large scale ocean circulation and to a too large fresh water in-
put in the north Atlantic (Swingedouw et al. 2006). At 45°N, the fresh water bias at depth cor-
395 responds to the Mediterranean outflow, which induces too low salinity at 1500 m. On the con-
trary, salinity is too high in the latitudes bands of 0°N-30°N and 15S-30°S, extending to about
1000 m.

In HiRes, the moisture content (not shown) is lower than in CTRL below 200 hPa and
higher above. The temperature follows this pattern, being colder than CTRL above 200 hPa,
400 and warmer below (**Fig. 4**), with an exception at high southern latitudes, where temperature
remains cooler at all altitudes. The equatorward shift of the atmospheric jet is present but
reduced when the atmospheric resolution increases, and so is the temperature bias. **Fig. 5**
synthetizes on a Taylor (2001) diagram the global correlation and the root mean square
difference between model and data, and shows that this shift in wind structure slightly
405 improves globally the ocean surface temperature and salinity. In high northern latitudes,
salinities are even smaller than in CTRL near the surface, but larger at depth, with a stronger
stratification.

The different equilibria between the two simulations are associated with slight differences
in the ocean and atmospheric heat transports (**Fig. 6**). In CTRL, the global ocean heat
410 transport is correct in the low latitudes, but is too weak north of 20°N and south of 20°S. The
value of $1.27 \cdot 10^{15}$ W at 24°N is lower than observation-based estimates of $1.8 \pm 0.3 \cdot 10^{15}$ W
(Ganachaud and Wunsch 2003). This weakness appears to be related to the Atlantic heat
transport (**Fig. 6e**). It reaches $0.68 \cdot 10^{15}$ W at 24°N in CTRL. Several estimates have been
415 made at this latitude, the lower range being provided by MacDonald (1998) with a
 $1.07 \pm 0.26 \cdot 10^{15}$ W estimate. The role of the ocean and of the atmosphere in redistributing heat
between the equator and the poles changes between the two experiments, with a more active
ocean in HiRes (**Fig. 6d**). This is attributed to a larger overturning transport in the Atlantic
(see below). In HiRes, the ocean heat transport north of 10°N reaches a maximum of
 $1.49 \cdot 10^{15}$ W, and an Atlantic maximum of $0.82 \cdot 10^{15}$ W.

420 The stream functions of the zonally integrated ocean flow of the present day equilibrium
simulations reflect the underestimation of the ocean heat transport (**Fig. 6**). Even though it is
in good qualitative agreement with observations in CTRL (e.g. Ganachaud and Wunsch 2003;
Talley et al. 2003), the maximum value of about 11 Sv ($1 \text{ Sv} \equiv 10^6 \text{ m}^3 \text{ s}^{-1}$) is too small. The
maximum strength of the AMOC increases in HiRes and reaches 15 Sv. This is still not suffi-
425 cient to ensure a realistic northward heat transport but it is not inconsistent with the observa-
tional estimates cited above. Apart from this intensification, the NADW cells are similar in
the two simulations. In particular, the cell reaches the same depth, approximately 3000 m. At
depth, the AABW is hardly affected by the change in atmospheric resolution. It is weak in
both cases.

430 Following Bryden and Imawaki (2001), we separate the oceanic heat transport between its
barotropic part (gyre heat transport) and its baroclinic part (overturning heat transport). The
gyre heat transport is very similar in the two simulations, with values of $0.19 \cdot 10^{15}$ W and
 $0.17 \cdot 10^{15}$ W for CTRL and HiRes respectively, while the overturning heat transport
significantly increases from $0.49 \cdot 10^{15}$ W in CTRL to $0.66 \cdot 10^{15}$ W in HiRes. The increase in

435 the Atlantic heat transport with increasing atmospheric resolution is therefore mostly due to
the improvement of the AMOC intensity (see section 7.2 for the explanations concerning this
improvement). Note that, according to Böning et al. (1995), every increase of 2 Sv in AMOC
is associate to an increase of $0.1 \cdot 10^{15}$ W in heat transport at 25°N . An AMOC intensity of
440 18 Sv at 25°N will be necessary to obtain a $1.1 \cdot 10^{15}$ W ocean heat transport. This value is in
agreement with Talley et al. (2003) estimates. It shows that in our simulations the bias in
AMOC intensity (8.3 Sv and 4.5 Sv at 25°N in CTRL and HiRes respectively) is consistent
with the bias in ocean heat transport.

6.4 Surface characteristics

Fig. 8a shows the difference between the simulated annual mean sea surface temperature
445 (SST) and the Reynolds (1988) climatology. Both simulations capture successfully the large-
scale patterns. The main shortcoming of CTRL is a cold bias at middle latitudes both in the
Atlantic and the Pacific oceans. The bias reaches 6°C in the North Atlantic, resulting from a
combination of a southward shift of the north Atlantic drift and the advection of cold water
from the north. At higher resolution (HiRes), the bias is strongly reduced in both oceans and
450 both hemispheres.

In the tropics, temperature and salinity biases are found in the eastern part of the basins in
the Atlantic and the Pacific, and along the continental boundaries in the Indian Ocean. This is
a typical bias in coupled ocean-atmosphere models (IPCC 2007, Fig. S8.1). It is associated
with insufficient resolution, which leads to a poor representation of the local wind stress and
455 the oceanic upwelling (Braconnot et al. 2007).

The combination of the cold bias at middle latitudes and the warm bias in the tropics is
associated to a stronger than observed equator-to-poles SST gradient. The gradient is
improved with enhanced atmospheric resolution, suggesting that increasing the resolution has
corrected some circulation errors. This differs from Hack et al. (2006) who find similar SST
460 error patterns and magnitudes in versions of the CCSM3 with atmospheric configurations T42
and T85 respectively.

The large-scale characteristics of precipitation (**Fig. 9**) in CTRL are detailed by Braconnot et
al. (2007). They are consistent with the temperature field. In January, precipitation north of
the equator in the eastern Pacific is too sluggish, with even less precipitation in HiRes. The
465 double ITCZ (intertropical convergence zone) at 4°S is present in both simulations, and is
stronger in HiRes. The structure of the South Pacific Convergence Zone is too zonal in both
simulations, penetrating too far toward the east Pacific. In the Atlantic, ITCZ precipitations
are too weak in January, particularly over the Amazon. In July, the ITCZ of CTRL is shifted
southward compared to observations. Its position is better represented in HiRes, with stronger
470 rainfall along the Africa coast. However, HiRes does not improve the monsoon rainfall over
Africa.

The large scale characteristics of the two simulations are summarized in Table and **Fig. 5**.
The larger improvement between CTRL and HiRes is obtained for sea ice in the southern
hemisphere. Other fields also benefits from measurable improvement. It concerns mainly the
475 dynamics of the atmosphere with the zonal wind stress and the 500 hPa filtered standard
deviation. Over the ocean, temperature benefits from larger improvements than salinity.

7 Regional characteristics and role of processes and feedback related to the atmospheric resolution.

This part focuses on the climate of specific regions to address the impact of the atmosphere
480 resolution on regional processes and feedbacks. In the North Atlantic, wind structure and vari-
ability have a strong impact over the ocean deep convection and thermohaline circulation. At
high southern latitudes, the Antarctic Circumpolar Current responds to the structure and

strength of winds. In the tropics, atmosphere resolution changes the seasonal cycle and the ENSO variability.

485 7.1 North Atlantic atmospheric circulation.

Most of the differences in the Atlantic sector between CTRL and HiRes may be attributed to differences in the winds. Mid-latitude climates are characterised by their day-to-day variability, especially in winter over the oceans and surrounding regions (Hoskins and Hodges 2002). The phenomena responsible for this variability are the weather systems that develop
490 over the Pacific and Atlantic oceans. They are responsible for a large part of the precipitation and of the equator-to-pole heat transport at these latitudes. Due to their typical size, of the order a thousand km, and to the present resolution of climate models, the representation of the variability associated with these weather systems is expected to be sensitive to resolution. For example, Dong and Valdes (2000) show that increasing the resolution from T21 to T42 leads
495 to major improvements of the storm-track representation, in particular in the amplitude of the storm-track. A further increase to T63 resolution does not yield such a strong effect, showing that T42 is a threshold resolution. The resolutions of our experiments, 96x72 and 144x96 straddle this threshold and we expect significant differences in the storm-track representation in the simulations.

500 **Fig. 10** shows the high-pass filtered 500 hPa geopotential height standard deviation computed from the NCEP/NCAR reanalyses and the CTRL and HiRes simulations. The filter is Hoskins et al. (2002) ‘poor-man filter’ retaining variability for periods smaller than 10 days. The figure shows that even at a medium resolution (CTRL) both storm-tracks are quite well represented. However, the Pacific storm-track is not strong enough and does not present
505 a secondary maximum near the American coast. In CTRL, the Atlantic storm-track has, as in the NCEP/NCAR reanalyses, a stronger maximum than the Pacific storm-track, but this maximum is smaller than in the reanalyses and the region of high variability does not extend as much to the Northeast, over the Norwegian Sea, as in the reanalyses. Both the amplitude and the longitudinal extent of the storm-tracks are better represented in HiRes. The Pacific
510 storm-track is even a little too strong. The Atlantic storm-track’s amplitude, on the other hand, is satisfactory but its eastern end tilts too much to the south compared to the reanalyses. The two simulations also differ over Siberia, with a larger variability, closer to the reanalyses, in the high resolution case.

The increased resolution therefore results in a better representation of the winter mid-latitude storm-tracks, which can relate to a slightly improved representation of the equator-to-pole transport shown on **Fig. 6**. Storm-tracks are related to equator-to-pole temperature
515 gradients through baroclinic instability theory. In section 6.4, we have shown that this gradient is too strong in the low resolution run, while it decreases and is more similar to the observed one in the high resolution run. So, the increase in storm-track variability in the high
520 resolution run is not related to an increased equator-to-pole thermal gradient, but rather, probably, to the resolution itself. The improvement of the representation of the precipitation over the East Atlantic could also be related to these improvements in the storm-tracks.

Another approach to diagnose the effect of the resolution on atmospheric circulation is to assess the North Atlantic Oscillation (NAO) variability in the two experiments. A large number
525 of spatial patterns and indices have emerged in studies of the northern hemisphere wintertime low-frequency variability. Recently, Quadrelli and Wallace (2004) have shown that they can all be almost fully retrieved by a linear combination of only two basis patterns: the leading two empirical orthogonal functions (EOF) of the monthly sea level pressure (SLP) field. The first two EOFs computed by a principal component analysis of the NCEP/NCAR reanalysis
530 SLP for the 1958-2007 period are shown on the left panels of **Fig. 11**. EOF1 is a quasi-zonally symmetric dipole between the polar and mid-latitude also called the Northern Annular

Mode or Arctic Oscillation. EOF2 on the other hand is a wavy pattern with a large centre of action over the Pacific and a weaker secondary wave train over Europe. The two EOFs are orthogonal by construction.

535 The first EOF of SLP for the CTRL and HiRes simulation is similar to the observed one (Fig. 11). Over the Atlantic sector, they all resemble the NAO pattern, although the structure is shifted slightly northward and stronger over Siberia in the simulations. The main difference is over the Pacific Ocean: in CTRL the EOF1 variance is concentrated in the Atlantic, whereas in HiRes and the reanalysis there is a secondary centre of action in the Pacific of
540 comparable amplitude. The second simulated EOF exhibit the dominant Pacific centre, shifted to the east in both cases. The wave train over the Atlantic is however better captured by HiRes, where it is in phase with the observed one, instead of phase quadrature for CTRL. These results can be summarized by Fig. 12, following Quadrelli and Wallace (2004): each simulated EOF is represented by a line whose projections on the horizontal and vertical axes
545 give the spatial correlation with the observed EOF 1 and 2, respectively. The HiRes EOFs reproduce almost perfectly the observed ones (the correlation of EOF 2 with NCEP/NCAR EOF2 is not perfect, because of the small shift of the Pacific centre, but the orthogonality with the EOF1 is conserved). For CTRL, EOF1 and 2 are rotated with respect to the NCEP ones: this reflects the poorer representation of the Pacific/Atlantic connections in this simulation.

550 There is therefore a strong improvement with resolution of the simulated variance in the Pacific, and its connection with the Atlantic sector. A possible reason is that the Pacific jet is stronger than the Atlantic one, and driven to a large extent by tropical heating. An even stronger jet, as found in lower resolution simulations, (not shown) will tend to trap eddies and destroy the positive feedback between eddies and jet fluctuations at the origin of the observed
555 low-frequency variability (Eichelberger and Hartmann 2007). This mechanism is consistent with a continuous decrease of the Pacific jet speed from CTRL to HiRes, and a corresponding increase in storm tracks amplitude and month-to-month sea level pressure variance. This is consistent with an improvement of the wind structure, and its effects on the gyre circulation (see below).

560 7.2 Oceanic circulation in the North Atlantic

The improvement of the atmospheric circulation in HiRes has a strong impact on the characteristics of the Atlantic Ocean, including the representation of sea ice cover, deep-water formation and thermohaline circulation. In the Northern Hemisphere, the sea ice concentration is overestimated in CTRL during wintertime in the Atlantic sector, with sea ice covering
565 the Labrador and Barents Seas (Fig. 14a). The maxima in ice thickness are situated north of the Canadian Archipelago and north of Greenland (Fig. 14a), in good agreement with observations (Bourke and McLaren 1992). A less realistic secondary maximum is present in the eastern Siberian Sea. On the other hand, a slight underestimation of the winter sea ice extent in the Okhotsk and Bering Seas is present (Fig. 14c). The underestimation of the ice extent is
570 still present in summer in HiRes in the North Atlantic, the GIN seas (Greenland-Icelandic-Nordic seas), and the Barents Sea (Fig. 14d). There is almost no difference with respect to CTRL in the Bering and Okhotsk Seas. HiRes has a more realistic ice thickness distribution in the Arctic, in particular in the eastern Siberian Sea where CTRL simulates an ice thickness higher than 6 m. The reduction of the bias there in HiRes is due to a better location of the Beaufort high in this model version. Indeed, in CTRL, the high pressure system in the Canadian Basin extends towards the North Siberia (not shown), resulting in onshore winds that transport sea ice towards the eastern Siberian Sea and induce a high sea ice accumulation there. DeWeaver and Bitz (2006) found the same type of reduction of model biases when comparing CCSM3 simulations at high and medium resolutions. They attribute this improve-

580 ment to a better representation of the fall and winter Arctic surface winds in the high resolution version of the model.

The sea ice off the Labrador Sea is reduced in HiRes, but still extends too far east. Because of a stronger northward oceanic heat transport in the northern North Atlantic (**Fig. 6e**), the overestimation in sea ice extent in the North Atlantic sector seen in CTRL is strongly
585 attenuated in HiRes, leading to a reasonable sea ice edge position in winter characterized by only small errors in the central Labrador Sea and north of Iceland. The improved ocean heat transport in HiRes is associated with differences in the location and intensity of deep-water formation. The model deep-water formation is characterised by two sites of deep convection in the North Atlantic (**Fig. 13**). One site is located in the Nordic Seas, as in the observations,
590 although the site is shifted to the south-east in the model as compared to observations and the maximum of the mixed layer depth is not deep enough (Swingedouw et al. 2006; Swingedouw et al. 2007). Both discrepancies are reduced in HiRes. The location of deep convection south of Iceland in both simulations is unrealistic, while there is no deep convection in the Labrador Sea in the model. As discussed in Swingedouw et al. (2007), this
595 is presumably due to an excess of fresh water input in the northern North Atlantic. As a result of this lack of convection in the Labrador Sea, this basin is fully covered by sea ice in winter, contrary to what is observed. The increase of atmospheric resolution induces a slight northward shift of the winter sea ice limit in the Labrador Sea, but this is still not sufficient to allow deep convection in the Labrador Sea. In agreement with the deepening of maximum
600 mixed layer depths in the northern North Atlantic, Atlantic MOC is stronger in HiRes and reaches 15 Sv (**Fig. 7**).

In both simulations and at both convection sites, an increase of sea surface density and mixed layer depth is correlated to increased sea surface salinity. In the model, deep convection is thus primarily driven by haline anomalies. SST is hardly correlated with sea
605 surface density anomalies in these areas (except south of Iceland in CTRL, but with a sign of correlation that would rather prevent deep-water formation).

Changing the resolution can affect the atmospheric dynamics and cloud distribution, which therefore can modify the water budget. Nonetheless, Hack et al. (2006) did not manage to correct the global precipitation bias by increasing horizontal resolution. Here we focus on the
610 atmospheric fresh water forcing of the Atlantic, north of 40°N for the different model resolutions in comparison with the data from ERA40 (Uppala et al. 2005) and UNESCO rivers data (Table). We notice that increasing the resolution does not significantly modify the total surface fresh water budget in the region analysed. A total bias of more than 0.1 Sv in comparison with the observations appears in both atmospheric resolutions. This bias is mostly
615 related to an incorrect budget of precipitation minus evaporation in the northern high latitudes. The difference in terms of salinity in the North Atlantic and AMOC between HiRes and CTRL is therefore not attributable to differences in surface fresh water forcing and is therefore certainly related to salt transport.

Following Wijffels et al. (1992), we separate the salinity transport into a gyre component primarily related to the barotropic part of the transport, and an overturning component related to the baroclinic part. The overturning salt transport depends on the AMOC intensity. It represents a classical positive feedback for the AMOC (Stommel 1961), which cannot be the trigger for an increase in salinity in the convection sites. Gyre salinity transport is related to the barotropic streamfunction, which strongly intensified when the atmosphere resolution
620 increases (not shown). This salinity transport related to the gyre is represented in **Fig. 15** for both resolutions in the Atlantic basin. The gyre salt transport reaches $15.9 \cdot 10^6 \text{ kg s}^{-1}$ at 50°N in HiRes and $9.9 \cdot 10^6 \text{ kg s}^{-1}$ in CTRL. This 50°N latitude is of paramount interest since the convection sites are very close and their salinity may therefore be highly sensitive to this
625

transport. Thus, the 59% enhancement in gyre salt transport certainly explains most of the increase in salinity observed in HiRes compared to CTRL.

7.3 Southern latitudes

In the southern hemisphere, the latitude of the observed zonal wind stress maximum is close to the latitude of the southern tip of America ($\sim 55^\circ$ S, see **Fig. 16**). In CTRL, the zonal wind stress is weaker than in observation, with a maximum at 43° S, and the location of the zero wind stress curl is shifted northward. The wind stress in the 55° S- 65° S latitude band is weak compare to observation. This yields a weak Antarctic Circumpolar Current (ACC, see **Fig. 16**), with a volume transport at Drake passage of 50 Sv, which is much lower than the observational estimate of 136.7 ± 7.8 Sv (Cunningham et al. 2003). In HiRes, the wind stress maximum is improved, and the latitude of the maximum is shifted southward at about 48° S. The zero of the wind stress curl is also shifted southward (not shown). Following (Russell et al. 2006), this yields a more southward location of the ACC in HiRes. The ACC is strengthened, with transport of 80 Sv through the Drake Passage.

In the Southern Ocean, both model versions tend to overestimate the amplitude of the seasonal cycle of the sea ice extent (**Fig. 14**), with sea ice almost vanishing in summer. On the other hand, because of a relatively high oceanic heat flux at the ice base, the winter sea ice thickness in the majority of the seasonal ice pack is quite low, with values lower than 50 cm. Higher values, up to 2m, are simulated in the Weddell Sea, along the Antarctic Peninsula and the Filchner-Ronne ice shelf, as well as in the eastern Ross Sea.

7.4 Seasonal and interannual variability in the tropics

This last part investigates the changes in the tropical regions. **Fig. 17** shows the annual mean and mean seasonal cycle of SST (annual mean removed) and of the zonal wind stress along the equator, compared to data and reanalyses (references in figure caption). The model is warmer than observed in all basins. In the Pacific and Indian oceans, the east-west SST gradient is correctly represented, with an exception near the Chile coast (**Fig. 17**, bottom). The Atlantic SST is too warm in the Gulf of Guinea. This is associated with a too flat Atlantic thermocline (Braconnot et al. 2007), too deep in the east, and to a lack of shallow clouds. The HiRes experiment has warmer SST in all basins, with an east-west gradient similar to CTRL. The zonal wind stress is correctly represented in intensity and east-west gradient in the Indian. In the Atlantic, winds are slightly too strong in the middle of the basin. In the Pacific, the east-west gradient is too strong, with a maximum near 160° west not well represented, and too strong eastward winds over the warm pool. The increase in resolution slightly improves the wind structure in the Pacific when compared to ERA40 reanalysis.

In the three basins, the seasonal cycle of SST and wind is correctly phased in both experiments, but the amplitudes are too low (**Fig. 17**). In the Atlantic, the maximum of SST variability is shifted toward the Brazilian coast. In the Pacific, the SST variability extends correctly from the east, but its westward extension is slightly underestimated. The SST is quite similar to observed ones, except near the Chile coast, where it is too warm. From November to January, southern hemisphere trade winds cross the equator, and a maximum of zonal winds is located around 150° W in ERA40 (**Fig. 17b**). In the two experiments, this maximum is not present (**Fig. 17d** and **f**). The northern hemisphere trade winds penetrate too far south (Braconnot et al. 2007, **Fig. 4b**), and the southern hemisphere trade winds do not cross the equator. This is consistent with the presence of the double ITCZ structure with a secondary maximum precipitation around 4° S. These low winds yield a reduction of the equatorial upwelling, and a spurious SST maximum (**Fig. 17a**, **c** and **e**) during this season. SST is well represented in the Indian sector. The resolution does not affect much the phasing and the position of the structures, but slightly improved the amplitude. For instance the

temperature maximum in April is improved in all basins. Compared to those of the other CMIP3 models, the seasonal cycle in the east Pacific in IPSL-CM4 is quite well represented, both in phase and amplitude (about 2.7 yrs vs. 4-5 yrs in observations, Guilyardi 2006).

680 The monthly standard deviation of SST (**Fig. 18a-c**) shows that the ENSO amplitude in CTRL is about right (1.0°C in Niño3¹ vs. 0.85°C for observations). Its structure extends too far to the west and is too confined around the equator (see the 0.40°C contour). This is classical bias of coupled GCMs which tend to have too strong mean zonal wind stress τ_x (**Fig. 18g** and **Fig. 2** of Guilyardi 2006). The zonal wind stress variability is too weak in the
685 equatorial band between 10°S and 10°N (about half of the value of the ERA40 reanalysis, see **Fig. 18g**). The coupling strength, which measures the intensity of the atmosphere dynamical response to a SST anomaly (mostly via the Bjerknes feedback) is key to El Niño development and amplification. It can be diagnosed in coupled GCMs as the slope of the *Anomaly of τ_x Niño4 = f(anomaly of SST_{Niño3})* relationship. Here, the weak wind stress variability in CTRL results
690 in a weak interannual coupling strength of $4.3 \cdot 10^{-3} \text{ N m}^{-2} \text{ K}^{-1}$ instead of $9.5 \cdot 10^{-3} \text{ N m}^{-2} \text{ K}^{-1}$ in the ERA40 reanalysis, (**Fig. 18h**, see also Guilyardi (**Fig. 18h**, see also Guilyardi 2006)). This weak coupling strength together with a right amplitude suggests that the processes damping ENSO in the model are underestimated. This can either be due atmosphere feedbacks (Philip and Van Oldenborgh 2006; Sun et al. 2006) or to ocean feedbacks (Fedorov 2007). Indeed,
695 for instance, the surface heat flux damping associated with ENSO in Niño3 is only $-5 \text{ W m}^{-2} \text{ K}^{-1}$ whereas it reached $-20 \text{ W m}^{-2} \text{ K}^{-1}$ in ERA40. The ENSO frequency, as measured by the peak of the Niño3 SSTA spectra, is too high in CTRL (about 2.7 yrs vs. 4-5 yrs in observations, Guilyardi 2006).

In HiRes, the amplitude of the SST anomaly standard deviation is even larger than in CTRL
700 (**Fig. 18c**) and reaches 1.2°C in Niño3. The zonal wind stress response is much improved compared to CTRL (**Fig. 18f, g**) even if it is still too weak. The coupling strength (**Fig. 18i**, $6.0 \cdot 10^{-3} \text{ N m}^{-2} \text{ K}^{-1}$) is consequently improved and, if we assume the damping feedbacks being the same (the atmosphere physical parameterisations of the two simulations are the same and the heat flux feedback in Niño3 is also weak in HiRes at $-6 \text{ W m}^{-2} \text{ K}^{-1}$), this can explain the
705 stronger ENSO amplitude via a stronger positive Bjerknes feedbacks. Three possible reasons can be put forward to explain the clear improvement of equatorial zonal wind stress variability in HiRes compared to CTRL (**Fig. 18e, f, g**). First the atmosphere has a better resolution and can then better respond to the ocean scale SST variability, confined in the $2^{\circ}\text{S}/2^{\circ}\text{N}$ wave guide. Second, the atmosphere has more degrees of freedom and scale
710 interactions can transfer more energy from synoptic and intra-seasonal scales to interannual scales (Guilyardi et al. 2004, for similar results with the SINTEX model). And third, the atmosphere can better react to the tropical instability waves in the equatorial east Pacific ocean, which act as a momentum sink for the atmosphere, thereby reduced the mean wind stress bias and allowing stronger interannual variability (Guilyardi 2006). The ENSO
715 frequency in HiRes has now a 3.5 yrs peak in addition to the 2.7 yrs of CTRL (not shown). These improvements agree with other studies in which the atmosphere resolution was enhanced (Guilyardi et al. 2004; Navarra et al. 2008).

Both CTRL and HiRes large ENSO amplitude suggest that the damping processes are too weak in the model. These can be either due to atmosphere radiative feedbacks (Sun et al.
720 2006) or ocean dissipation (Fedorov 2007) and further work is needed to elucidate the origin of this bias. In any case, it seems that CTRL is getting the right ENSO amplitude for the wrong reasons, i.e. both too weak Bjerknes zonal wind/SST feedback and too weak damping. The combined effect of this biases can also explain why the model cannot develop full blown

¹ Niño 3 is the 5°S - $5^{\circ}\text{N}/120^{\circ}\text{W}$ - 170°W region. Niño4 is the 5°S - $5^{\circ}\text{N}/160^{\circ}\text{E}$ - 150°W region.

725 large thermocline events and is therefore locked into a SST mode, favouring higher than
observed ENSO frequency (2 year dominant peak, see Guilyardi 2006).

8 Conclusion

This manuscript describes the version 4 of the IPSL coupled ocean-atmosphere model. Specific care was put to have local and global conservation of heat and water fluxes. The heat flux budget confirms this closure, which allows long-term climate simulations, needed for
730 studying processes of the present climate variability as well as paleoclimates.

The comparison of two versions of the coupled ocean-atmosphere model with two different atmospheric resolutions allows us to investigate the interactions and feedbacks between the atmospheric dynamics and the global and local climate. The control simulation corresponds to the IPSL reference sent to the WCRP/CMIP3 IPCC 2007 database (Meehl et al. 2007). It is
735 compared with a simulation with higher resolution. The adjustment phases of the two resolutions are very similar, with the same characteristic timescale of adjustments. The global equilibrium is slightly different between the two versions. At higher resolution, the snow cover and the sea ice cover at high latitudes are reduced, with a lower albedo, inducing a warmer atmosphere. This warming propagates to the surface ocean, and penetrates in the
740 ocean down to 2000 m in the southern subtropics and in the high latitudes of both hemispheres.

In a first approximation, model biases are close to biases found in atmosphere alone simulations (Hourdin et al. 2006). The increase in resolution improves several aspect of the simulated climate in atmosphere alone and coupled simulations, like the storm-tracks, the
745 characteristics of the North-Atlantic Oscillation and the seasonal and inter-annual variability in the tropics. On the contrary, the African monsoon remains poorly simulated at both resolutions.

The increase in atmospheric resolution improves the mid and high latitudes wind (mean state and variability). The better structure of surface winds strengthen the surface ocean
750 circulation, transporting more salt towards the high latitudes of the Atlantic ocean, reducing the sea ice cover, and increasing the oceanic convection and the AMOC. However, the increase in gyre salt transport is not sufficient to set deep convection in the Labrador Sea, which is related to the excess of precipitation minus evaporation north of 40°N. This explains the remaining bias in the AMOC intensity, which is therefore certainly related to an excess of
755 precipitation minus evaporation north of 40°N.

In the tropics the model performs reasonably well, for both seasonal and interannual variability. ENSO amplitude is about right in the control simulation, and becomes too large at higher resolution. The dynamical coupling strength between SST and wind anomalies is too weak in the control, and is strongly improved at higher resolution. The damping processes are
760 too weak for both atmosphere resolutions, and further work is needed to elucidate why.

We conclude that the increase in horizontal resolution for the atmosphere in the climate model IPSL-CM4 leads to substantial improvements in atmospheric circulation, but also in thermohaline circulation and sea ice cover pattern. The choice of the atmospheric model resolution for the next IPCC report needs to be evaluated carefully in order to find the best
765 compromise between representation of climate and computational costs. The present study actually shows that there may exist thresholds in atmospheric resolution that leads to large improvements for the climate system modelling. New simulations at higher atmospheric resolutions (144x144, 192x144, 192x192, ...) will be considered.

9 Appendix

9.1 Interface for coupling the turbulent fluxes

A first standard interface for the coupling between the surface and the atmosphere was proposed by the PILPS project (Polcher et al. 1998; 2005). A drawback of the proposed approach is that the separation between the solving of the turbulent fluxes in the boundary layer and the solving of the temperature by the surface model is not complete. Indeed, the time evolution of the first atmospheric level variables (Polcher et al. 1998) is a function of the surface flux, but also of some surface coefficients. We overcome this difficulty by rewriting the discretized form of the vertical diffusion equation of the first atmospheric level and by considering explicitly the flux $F_{X,1/2}^{t+\delta t}$ between layer 1 and the surface:

$$\frac{X_1^t - X_1^{t+\delta t}}{\delta t} = \frac{1}{\delta z_1} \left(K_{X,3/2} \frac{X_2^{t+\delta t} - X_1^{t-\delta t}}{\delta z_{3/2}} - F_{X,1/2}^{t+\delta t} \right) \quad \text{Eq. 1}$$

and

$$F_{X,1/2}^{t+\delta t} = K_{X,1/2} \frac{X_1^{t+\delta t} - X_0^{t+\delta t}}{\delta z_{1/2}} \quad \text{Eq. 2}$$

Variables X stands for the dry static energy, the specific humidity or the wind speed, $F_{X,k-1/2}$ is the flux of X at interface $k-1/2$ (between level k and $k-1$), $K_{X,k-1/2}$ is the vertical diffusion coefficient for variable X at this level; δz_k is the thickness of layer k and δz_{k+1} is the distance between the centres of layers k and $k-1$.

9.1.1 In the boundary layer

To solve the vertical diffusion equation in the boundary layer, each variable of level k is written as a function of the variable of the level below $k-1$, for all levels except level 1:

$$X_k^{t+\delta t} = A_{X,k} X_{X,k-1}^{t+\delta t} + B_{X,k} \quad \text{for } k \geq 2 \quad \text{Eq. 3}$$

For level 1, $X_2^{t+\delta t}$ may be suppressed from Eq. 1, using:

$$A_{X,1} = -\frac{\delta t}{\delta z_1 C_{X,1}} \quad \text{Eq. 5}$$

and

$$X_1^{t+\delta t} = A_{X,1} F_{X,1/2}^{t+\delta t} + B_{X,1} \quad \text{Eq. 4}$$

$$A_{X,1} = -\frac{\delta t}{\delta z_1 C_{X,1}} \quad \text{Eq. 5}$$

$$B_{X,1} = \left(X_1^t + \frac{\delta t K_{X,3/2}}{\delta z_1 \delta z_{3/2}} \right) \frac{1}{C_{X,1}} \quad \text{Eq. 6}$$

and

$$C_{X,1} = 1 + \frac{\delta t K_{X,3/2}}{\delta z_1 \delta z_{3/2}} (1 - A_{X,2}) \quad \text{Eq. 7}$$

790 One may verify that Eq. 4-Eq. 7 make only use of the flux with surface $F_{X,1/2}^{t+\delta t}$ and of atmospheric variables above layer 1. There is no use of surface variable or surface coefficient. For each variable X , variables $X_{X,1}$, $A_{X,1}$ and $B_{X,1}$ are transmitted by the boundary layer model to the surface model.

9.1.2 In the surface model

795 The surface model has to compute the surface flux $F_{X,1/2}^{t+\delta t}$ for each variable X . For the temperature and the humidity at the surface, the new values $X_1^{t+\delta t}$ are computed (if required) through the energy and water budget of the surface. The coupling between atmosphere and surface being implicit, a relationship between $F_{X,1/2}^{t+\delta t}$ and $X_0^{t+\delta t}$ is required. This is obtained by combining Eq. 2-Eq. 4:

$$F_{X,1/2}^{t+\delta t} = \frac{K_{X,1/2}}{\delta z_{1/2} - K_{X,1/2} A_{X,1}} (B_{X,1} - X_0^{t+\delta t}) \quad \text{Eq. 8}$$

800 9.2 Decomposition of the oceanic heat transport

The oceanic heat transport across a latitude λ due to advection is computed as:

$$F = \int_{z=0}^{\text{bottom}} \int \rho C_p T v r_a \cos(\lambda) d\varphi dz \quad \text{Eq. 9}$$

805 c mass, C_p the heat capacity per mass unit, T the temperature, v the northward velocity, r_a the Earth radius, j the longitude and z the depth. T and z the depth. T and v are separated in $T = \overline{T} + T'$ and $v = \overline{v} + v'$, where the overline denotes the latitudinal average, and prime the latitudinal anomaly. The transport can be decomposed (2001) as:

$$F = \iint \rho C_p \overline{T} \overline{v} r_a \cos(\lambda) d\varphi dz + \iint \rho C_p T' v' r_a \cos(\lambda) d\varphi dz \quad \text{Eq. 10}$$

The first term is the overturning transport and the second one the gyre transport.

9.3 Time filtering of snow accumulation on land ice.

810 On land-ice surface, the local snow mass is limited to $3,000 \text{ kg m}^{-2}$. At each time-step, the snow mass over this limit $C(t)$ is computed. The calving C^* send to ocean is computed as a filtered snow mass $C(t) = (\Delta t/\tau).C(t) + (1-\Delta t/\tau).C^*(t-1)$, where Δt is the model time step and τ is a characteristic time, set to ten years in all experiments.

815 **Acknowledgements** We thank all the people at Institut Pierre Simon Laplace, Institut d'Astronomie Georges Lemaître and Centre Européen de Recherche et de Formation Avancée en Calcul Scientifique who participate to the development of the model components, the assembling of the climate model, and the development of compilation, running and post-processing environments. Computer time was provided by Centre National de la Recherche Scientifique and Commissariat à l'Energie Atomique. This work is a contribution to the European project ENSEMBLES (Project no. GOCE-CT-2003-505539) and to the French project MissTerre (LEFE-EVE). The authors wish to acknowledge use of the Ferret program for analysis and graphics in this paper. Ferret is a product of NOAA's Pacific Marine Environmental Laboratory (information is available at <http://ferret.pmel.noaa.gov/Ferret>).

10 References

- Alkama R, Kageyama M and Ramstein G (2006). Freshwater discharges in a simulation of the Last Glacial Maximum climate using improved river routing. *Geophys Res Let* 33(21):-
- 825 Andrich P (1988), OPA - A multitasked Ocean General Circulation Model - Reference Manual, 60 pages, LODYC - Université Paris VI - France
- Ball JT, Woodrow TE and Berry JA (1987). A model predicting stomatal conductance and its contribution to the control of photosynthesis under different environmental conditions. *Prog in Photosynth* 4:221-224
- Barkstrom BR (1984). The Earth Radiation Budget Experiment (ERBE). *Bul Am Met Soc* 65:1170-1185
- 830 Beckman A (1998). The representation of bottom boundary layer processes in numerical ocean circulation models. *Ocean Modeling and Parametrization*. EP Chassignet and J Verron. Norwell, Mass., Kluwer Acad.
- Boning CW, Holland WR, Bryan FO, Danabasoglu G and McWilliams JC (1995). An Overlooked Problem in Model Simulations of the Thermohaline Circulation and Heat-Transport in the Atlantic-Ocean. *J Clim* 8(3):515-523
- 835 Bony S and Emanuel KA (2001). A parameterization of the cloudiness associated with cumulus convection; Evaluation using TOGA COARE data. *J Atmos Sc* 58(21):3,158-3,183
- Bourke RH and McLaren AS (1992). Contour Mapping of Arctic Basin Ice Draft and Roughness Parameters. *Journal of Geophysical Research-Oceans* 97(C11):17,715-17,728
- Braconnot P (1998), Tests de sensibilité avec le modèle d'atmosphère du LMD en vue d'améliorer le couplage avec l'océan, note technique IPSL 0076, 39 pp, IPSL
- 840 Braconnot P, Hourdin F, Bony S, Dufresne J-L, Grandpeix J-Y and Marti O (2007). Impact of different convective cloud schemes on the simulation of the tropical seasonal cycle in a coupled ocean-atmosphere model. *Clim Dyn* 29:501-520, DOI 10.1007/s00382-007-0244-y
- Braconnot P, Joussaume S, Marti O and de Noblet N (1999). Synergistic feedbacks from ocean and vegetation on the African monsoon response to mid-Holocene insolation. *Geophys Res Let* 26(16):2481-2484
- 845 Braconnot P, Joussaume S, Marti O and de Noblet N (2000). Impact of ocean and vegetation feedback on 6ka monsoon changes. Third PMIP Workshop, La Huardière, Canada, WCRP
- Braconnot P and Marti O (2003). Impact of precession on monsoon characteristics from coupled ocean atmosphere experiments: changes in Indian monsoon and Indian ocean climatology. *Marine Geology* 201(1-3):23-34
- 850 Braconnot P, Marti O and Joussaume S (1997). Adjustment and feedbacks in a global coupled ocean-atmosphere model. *Clim Dyn* 13(7-8):507-519
- Braconnot P, Otto-Bliesner B, Harrison S, Joussaume S, Peterchmitt JY, Abe-Ouchi A, Crucifix M, Driesschaert E, Fichefet T, Hewitt CD, Kageyama M, Kitoh A, Laine A, Loutre MF, Marti O, Merkel U, Ramstein G, Valdes P, Weber SL, Yu Y and Zhao Y (2007). Results of PMIP2 coupled simulations of the Mid-Holocene and Last Glacial Maximum - Part 1: experiments and large-scale features. *Climate of the Past* 3(2):261-277
- 855 Bryden HL and Imawaki S (2001). Ocean heat transport. *Ocean circulation and climate: observing and modelling the global ocean*. G Siedler, JA Church and J Gould. San Diego, Academic Press:445-474
- Collatz GJ, Ribas-Carbo M and Berry JA (1992). Coupled Photosynthesis-Stomatal Conductance Model for Leaves of C4 Plants. *Austral J of Plant Physiol* 19(5):519-538
- 860 Cunningham SA, Alderson SG, King BA and Brandon MA (2003). Transport and variability of the Antarctic Circumpolar Current in Drake Passage. *Journal of Geophysical Research-Oceans* 108(C5), 10.1029/2001JC001147
- de Boyer Montégut CD, Madec G, Fischer AS, Lazar A and Iudicone D (2004). Mixed layer depth over the global ocean: An examination of profile data and a profile-based climatology. *Journal of Geophysical Research-Oceans* 109(C12), 10.1029/2004JC002378
- 865 DeWeaver E and Bitz CM (2006). Atmospheric circulation and its effect on Arctic sea ice in CCSM3 simulations at medium and high resolution. *J Clim* 19(11):2415-2436
- Dong BW and Valdes PJ (2000). Climates at the last glacial maximum: Influence of model horizontal resolution. *J Clim* 13(9):1554-1573
- 870 Ducoudré N, Laval K and Perrier A (1993). SECHIBA, a New Set of Parameterizations of the Hydrologic Exchanges at the Land-Atmosphere Interface within the LMD Atmospheric General Circulation Model. *J Clim* 6:248-273
- Dufresne J-L and Grandpeix J-Y (1996), Raccordement des modèles thermodynamiques de glace, d'océan et d'atmosphère, Note Interne 205, Laboratoire de Météorologie Dynamique
- 875 Dufresne JL, Friedlingstein P, Berthelot M, Bopp L, Ciais P, Fairhead L, Le Treut H and Monfray P (2002). On the magnitude of positive feedback between future climate change and the carbon cycle. *Geophys Res Let* 29(10), DOI 10.1029/2001GL013777
- Dufresne JL, Quaas J, Boucher O, Denvil S and Fairhead L (2005). Contrasts in the effects on climate of anthropogenic sulfate aerosols between the 20th and the 21st century. *Geophys Res Let* 32(21), 10.1029/2005GL023619
- 880

- Eichelberger SJ and Hartmann DL (2007). Zonal jet structure and the leading mode of variability. *J Clim* 20(20):5149-5163
- Emanuel KA (1991). The Theory of Hurricanes. *Ann Rev of Fluid Mech* 23:179-196
- 885 Farquhar GD, Caemmerer SV and Berry JA (1980). A Biochemical-Model of Photosynthetic CO₂ Assimilation in Leaves of C-3 Species. *Planta* 149(1):78-90
- Fedorov AV (2007). Net energy dissipation rates in the tropical ocean and ENSO dynamics. *J Clim* 20(6):1108-1117
- Fichefet T and Morales-Maqueda AM (1997). Sensitivity of a global sea ice model to the treatment of ice thermodynamics and dynamics. *Journal of Geophysical Research* 102(C6):12609-12646
- 890 Fichefet T and Morales-Maqueda AM (1999). Modelling the influence of snow accumulation and snow-ice formation on the seasonal cycle of the Antarctic sea-ice cover. *Clim Dyn* 15(4):251-268
- Filiberti M-A, Dufresne J-L and Grandpeix J-Y (2001). Reference manual for IGLOO Sea Ice Model. Note technique du Pôle de modélisation, Institut Pierre-Simon Laplace:35 pp
- 895 Fouquart Y and Bonnel B (1980). Computations of solar heating of the Earth's atmosphere: a new parametrization. *Contrib Atmos Phys* 53:35-62
- Friedlingstein P, Bopp L, Ciais P, Dufresne JL, Fairhead L, LeTreut H, Monfray P and Orr J (2001). Positive feedback between future climate change and the carbon cycle. *Geophys Res Let* 28(8):1543-1546
- Ganachaud A and Wunsch C (2000). Improved estimates of global ocean circulation, heat transport and mixing from hydrographic data. *Nature* 408(23 November):453-457
- 900 Ganachaud A and Wunsch C (2003). Large-scale ocean heat and freshwater transport during the World ocean circulation experiment. *J Clim* 16:696-705
- Gloersen P and Campbell WJ (1991). Recent variations in Arctic and Antarctic sea-ice covers. *Nature* 352:33-36
- Guilyardi E (2006). El Niño-mean state-seasonal cycle interactions in a multi-model ensemble. *Clim Dyn* 26(4):329-348
- 905 Guilyardi E, Gualdi S, Slingo JM, Navarra A, Delecluse P, Cole J, Madec G, Roberts M, Latif M and Terray L (2004). Representing El Niño in coupled ocean-atmosphere GCMs: The dominant role of the atmospheric component. *J Clim* 17(24):4623-4629
- Guilyardi E, Madec G and Terray L (2001). The role of lateral ocean physics in the upper ocean thermal balance of a coupled ocean-atmosphere GCM. *Clim Dyn* 17(8):589-599
- 910 Hack JJ, Caron JM, Danabasoglu G, Oleson KW, Bitz C and Truesdale JE (2006). CCSM-CAM3 climate simulation sensitivity to changes in horizontal resolution. *J Clim* 19(11):2267-2289
- Hack JJ, Caron JM, Yeager SG, Oleson KW, Holland MM, Truesdale JE and Rasch PJ (2006). Simulation of the global hydrological cycle in the CCSM Community Atmosphere Model version 3 (CAM3): Mean features. *J Clim* 19(11):2199-2221
- 915 Hagemann S and Dumenil L (1998). A parametrization of the lateral waterflow for the global scale. *Clim Dyn* 14(1):17-31
- Hibler WDI (1979). A dynamic thermodynamic sea ice model. *J Phys Oceanogr* 9:815-846
- Hoskins BJ and Hodges KI (2002). New perspectives on the Northern Hemisphere winter storm tracks. *J Atmos Sc* 59(6):1041-1061
- 920 Hourdin F, Issartel JP, Cabrit B and Idelkadi A (1999). Reciprocity of atmospheric transport of trace species. *Comptes Rendus de L'Académie des Sciences, Serie II, Fascicule a, Sciences de la Terre et des Planètes* 329(9):623-628
- Hourdin F, Musat I, Bony S, Braconnot P, Codron F, Dufresne JL, Fairhead L, Filiberti MA, Friedlingstein P, Grandpeix JY, Krinner G, Levan P, Li ZX and Lott F (2006). The LMDZ4 general circulation model: climate performance and sensitivity to parametrized physics with emphasis on tropical convection. *Clim Dyn* 27(7-8):787-813
- 925 IPCC (2007). *Climate Change 2007 - The Physical Science Basis, Contribution of Working Group I to the Fourth Assessment Report of the IPCC*, 981 pp, IPCC, Geneva
- Jakobsson M, Cherkis NZ, Woodward J, Macnab R and Coakley B (2000). New grid of Arctic bathymetry aids scientists and mapmakers. *EOS Transactions* 81(9):89, 93, 96
- 930 Jones PW (1999). First- and second-order conservative remapping schemes for grid in spherical coordinates. *Mont Weath Rev* 127(9):2204-2210
- Kageyama M, Peyron O, Pinot S, Tarasov P, Guiot J, Jousseaume S and Ramstein G (2001). The Last Glacial Maximum climate over Europe and western Siberia: a PMIP comparison between models and data. *Clim Dyn* 17(1):23-43
- 935 Kageyama M, Valdes PJ, Ramstein G, Hewitt C and Wyputta U (1999). Northern hemisphere storm tracks in present day and last glacial maximum climate simulations: A comparison of the European PMIP models. *J Clim* 12(3):742-760
- 940 Kalnay E, Kanamitsu M, Kistler R, Collins W, Deaven D, Gandin L, Iredell M, Saha S, White G, Woollen J, Zhu Y, Chelliah M, Ebisuzaki W, Higgins W, Janowiak J, Mo KC, Ropelewski C, Wang J, Leetmaa A,

- Reynolds R, Jenne R and Joseph D (1996). The NCEP/NCAR 40-year reanalysis project. *Bul Am Met Soc* 77(3):437-471
- Khodri M, Cane MA, Kukla G, Gavin J and Braconnot P (2005). The impact of precession changes on the Arctic climate during the last interglacial-glacial transition. *Earth Planet Sci Let* 236(1-2):285-304
- 945 Krinner G, Genthon C, Li Z-X and Le Van P (1997). Studies of the Antarctic climate with a stretched-grid general circulation model. *Journal of Geophysical Research* 102:13731-13745
- Krinner G, Viovy N, de Noblet-Ducoudré N, Ogée J, Polcher J, Friedlingstein P, Ciais P, Sitch S and Prentice IC (2005). A dynamic global vegetation model for studies of the coupled atmosphere-biosphere system. *Glob Biogeochem Cycle* 19(1), doi:10.1029/2003GB002199
- 950 L'Heveder B (1999). Variabilité saisonnière et interannuelle des glaces de mer en Arctique: influence des interactions avec l'atmosphère. PhD, Paris VI, pp 132
- Le Clainche Y (1996). Modélisation du ruissellement dans un modèle couplé, Tech. rep., LSCE, Saclay
- Le Treut H and Li Z-X (1991). Sensitivity of an atmospheric general circulation model to prescribed SST changes: Feedback effect associated with the simulation of the cloud optical properties. *Clim Dyn* 5:175-187
- 955 Levitus S (1982). Climatological atlas of the world ocean, 13, 173 pp, NOAA/ERL GFDL, Washington D.C
- Lott F (1997). The transient emission of propagating gravity waves by a stably stratified shear layer. *Quart J Roy Met Soc* 123(542):1603-1619
- Lott F (1999). Alleviation of stationary biases in a GCM through a mountain drag parameterization scheme and a simple representation of mountain lift forces. *Mont Weath Rev* 127(5):788-801
- 960 Lythe MB and Vaughan DG (2001). BEDMAP: a new ice thickness and subglacial topographic model of Antarctica. *Journal of Geophysical Research - Solid Earth* 106:11335-11351
- MacDonald A (1998). The global ocean: a hydrographic estimate and regional analysis. *Prog Oceanogr* 41:281-382
- 965 Madec G, Delecluse P, Imbard M and Levy C (1997). OPA version 8.1 Ocean General Circulation Model Reference Manual, 3, 91 pp, LODYC, Technical Report
- Madec G and Imbard M (1996). A global ocean mesh to overcome the North Pole singularity. *Clim Dyn* 12(6):381-388
- Marti O, Braconnot P, Bellier J, Benshila R, Bony S, Brockmann P, Cadule P, Caubel A, Denvil S, Dufresne JL, Fairhead L, Filiberti M-A, Foujols M-A, Fichefet T, Friedlingstein P, Goosse H, Grandpeix JY, Hourdin F, Krinner G, Lévy C, Madec G, Musat I, de Noblet N, Polcher J and Talandier C (2005). The new IPSL climate system model: IPSL-CM4, Note du Pôle de Modélisation 26, 84 pp, Institut Pierre Simon Laplace, Paris
- 970 Meehl GA, Covey C, Delworth TL, Latif M, McAvaney B, Mitchell JFB, Stouffer RJ and Taylor KE (2007). The WCRP CMIP3 multimodel dataset: a new era in climate change research. *Bul Am Met Soc* 88(9):1383-1394, DOI:10.1175/BAMS-88-9-1383
- Morcrette JJ, Smith L and Fouquart Y (1986). Pressure and temperature dependence of the absorption in longwave radiation parametrizations. *Contrib Atmos Phys* 59(4):455-469
- Murray RJ (1996). Explicit generation of orthogonal grids for ocean models. *J Comput Phys* 126:251-273
- 980 Navarra A, Gualdi S, Masina S, Behera S, Luo JJ, Masson S, Guilyardi E, Delecluse P and Yamagata T (2008). Atmospheric horizontal resolution affects tropical climate variability in coupled models. *J Clim* 21(4):730-750
- Ngo-Duc T, Polcher J and Laval K (2005). A 53-year forcing data set for land surface models. *J Geophys Res (Atm)* 110(D6), 10.1029/2004JD005434
- 985 Philip S and Van Oldenborgh GJ (2006). Shifts in ENSO coupling processes under global warming. *Geophys Res Let* 33(11):-, doi:10.1029/2006GL026196
- Pinot S, Ramstein G, Harrison SP, Prentice IC, Guiot J, Stute M and Joussaume S (1999). Tropical paleoclimates at the Last Glacial Maximum: comparison of Paleoclimate Modeling Intercomparison Project (PMIP) simulations and paleodata. *Clim Dyn* 15(11):857-874
- 990 Polcher J, McAvaney B, Viterbo P, Gaertner MA, Hahmann A, Mahfouf JF, Noilhan J, Phillips T, Pitman A, Schlosser CA, Schulz JP, Timbal B, Verseghy D and Xue Y (1998). A proposal for a general interface between land surface schemes and general circulation models. *Glob Planet Change* 19(1-4):261-276
- Quadrilli R and Wallace JM (2004). A simplified linear framework for interpreting patterns of Northern Hemisphere wintertime climate variability. *J Clim* 17(19):3728-3744
- 995 Rayner NA, Parker DE, Horton EB, Folland CK, Alexander LV, Rowell DP, Kent EC and Kaplan A (2003). Global analyses of sea surface temperature, sea ice, and night marine air temperature since the late nineteenth century. *Journal of Geophysical Research-Atmospheres* 108(D14), 10.1029/2002JD002670
- Reynolds RW (1988). A real time global sea-surface temperature analysis. *J Clim* 1:75-86
- Roulet G and Madec G (2000). Salt conservation, free surface, and varying levels: a new formulation for ocean general circulation models. *J Geophys Res (Oceans)* 105(C10):23,927-23,942
- 1000

- Russell J, Stouffer RJ and Dixon KW (2006). Intercomparison of the Southern Ocean circulations in IPCC coupled control simulations. *J Clim* 19:4560-4575
- Sadourny R and Laval K (1984). January and July performance of the LMD general circulation model. New perspectives in climate Modelling, Developments in Atmospheric Science. AL Berger and C Nicolis. 16:173-198
- 1005 Smith WHF and Sandwell DT (1997). Global sea-floor topography from satellite altimetry and ship depth sounding. *Science* 277:1956-1952
- Steele M, Morley R and Ermold W (2001). PHC: A global ocean hydrography with a high-quality Arctic Ocean. *J Clim* 14(9):2079-2087
- 1010 Stommel H (1961). Thermohaline Convection with 2 Stable Regimes of Flow. *Tellus* 13(2):224-230
- Sun DZ, Zhang T, Covey C, Klein SA, Collins WD, Hack JJ, Kiehl JT, Meehl GA, Held IM and Suarez M (2006). Radiative and dynamical feedbacks over the equatorial cold tongue: Results from nine atmospheric GCMs. *J Clim* 19(16):4059-4074
- Swingedouw D, Braconnot P, Delecluse P, Guilyardi E and Marti O (2007). The impact of global freshwater forcing on the thermohaline circulation: adjustment of North Atlantic convection sites in a CGCM. *Clim Dyn* 28(2-3):291-305
- 1015 Swingedouw D, Braconnot P and Marti O (2006). Sensitivity of the Atlantic Meridional Overturning Circulation to the melting from northern glaciers in climate change experiments. *Geophys Res Let* 33(7), doi:10.1029/2006GL025765
- 1020 Talley LD, Reid JL and Robbins PE (2003). Data-based meridional overturning streamfunctions for the global ocean. *J Clim* 16(19):3213-3226
- Taylor KE (2001). Summarizing multiple aspects of model performance in a single diagram. *Journal of Geophysical Research-Atmospheres* 106(D7):7183-7192
- Tiedtke M (1989). A comprehensive mass flux scheme for cumulus parameterization in large-scale models. *Mont Weath Rev* 117:1179-1800
- 1025 Timmermann R, Goosse H, Madec G, Fichefet T, Ethé C and Dulière V (2004). On the representation of high latitude processes in the ORCA-LIM global coupled sea ice-ocean model. *Ocean Mod* 8(1-2):175-201
- Trenberth KE and Caron JM (2001). Estimates of meridional atmosphere and ocean heat transports. *J Clim* 14(16):3433-3443
- 1030 UNESCO (1985), Discharge of selected rivers of the world, v.3, pt. 4: mean monthly and extreme discharges, 1976-1979, 5, 126 pp, UNESCO
- Uppala SM, Kallberg PW, Simmons AJ, Andrae U, Bechtold VD, Fiorino M, Gibson JK, Haseler J, Hernandez A, Kelly GA, Li X, Onogi K, Saarinen S, Sokka N, Allan RP, Andersson E, Arpe K, Balmaseda MA, Beljaars ACM, Van De Berg L, Bidlot J, Bormann N, Caires S, Chevallier F, Dethof A, Dragosavac M, Fisher M, Fuentes M, Hagemann S, Holm E, Hoskins BJ, Isaksen I, Janssen PAEM, Jenne R, McNally AP, Mahfouf JF, Morcrette JJ, Rayner NA, Saunders RW, Simon P, Sterl A, Trenberth KE, Untch A, Vasiljevic D, Viterbo P and Woollen J (2005). The ERA-40 re-analysis. *Quart J Roy Met Soc* 131(612):2961-3012
- Valcke S (2006), OASIS3 User Guide (prism_2-5), PRISM support initiative 3, 68 pp
- Van Leer B (1977). Towards the ultimate conservative difference scheme: IV A new approach to numerical convection. *J Comput Phys* 23:276-299
- 1040 Verant S, Laval K, Polcher J and De Castro M (2004). Sensitivity of the continental hydrological cycle to the spatial resolution over the Iberian Peninsula. *J of Hydrometeorology* 5(2):267-285
- Wijffels SE, Schmitt RW, Bryden HL and Stigebrandt A (1992). Transport of Fresh-Water by the Oceans. *J Phys Oceanogr* 22(2):155-162
- 1045 Wunsch C (2005). The total meridional heat flux and its oceanic and atmospheric partition. *J Clim* 18(21):4374-4380
- Xie PP and Arkin PA (1997). Global precipitation: A 17-year monthly analysis based on gauge observations, satellite estimates, and numerical model outputs. *Bul Am Met Soc* 78(11):2539-2558
- 1050

11 List of tables

Table 1 Concentration of greenhouse gases used in all experiments 24

Table 2 Global averages of heat fluxes and albedos. Atmospheric green house effect is computed as $\sigma T_s^4 - LW_{top}$, where σ is Stefan’s constant, T_s is the surface temperature and LW_{top} the net long wave flux at top of atmosphere..... 24

1055

Table 3 Drift of temperature and salinity in the deep ocean, averaged between 1000 m and bottom, for global ocean and Atlantic, Pacific and Indian basins. The drift is computed from basin averages from year 401 to 500, the period being used for all analyses..... 25

Table 4 Global averages of key climatic variables, synthesizing the information provided in the figure listed in the rightmost column..... 25

1060

Table 5 Comparison of the fresh water budget (in mSv $\equiv 10^3 \text{ m}^3 \text{ s}^{-1}$) of different simulations with climatology of continental runoff discharge from UNESCO and evaporation minus evaporation (E-P) from ERA40 (Uppala et al. 2005), north of 40°N in the Atlantic and Arctic Ocean. 25

1065

12 Tables

CO ₂	CH ₄	N ₂ O	CFC11	CFC12
348 ppm	1650 ppb	306 ppb	280 ppt	484 ppt

Table 1 Concentration of greenhouse gases used in all experiments

Variable	CTRL	HiRes	HiRes - CTRL
Air temperature at 2m (°C)	12.89	13.85	0.87
Net heat budget at TOA (W m ⁻²)	-0.068	-0.125	-0.06
Net short wave at TOA (W m ⁻²)	236.5	239.7	3.18
Net long wave at TOA (W m ⁻²)	236.6	239.8	3.24
Net heat budget at surface (W m ⁻²)	-0.17	-0.15	0.015
Net short wave at surface (W m ⁻²)	168.8	171.9	3.17
Net long wave at surface (W m ⁻²)	-67.4	-67.8	-0.40
Sensible heat flux (W m ⁻²)	-26.1	-25.9	0.25
Latent heat flux (W m ⁻²)	-75.6	-78.7	-3.02
Planetary albedo	0.34	0.33	-0.01
Surface albedo	0.16	0.15	-0.01
Precipitable water (g kg ⁻¹)	22.74	23.87	1.13
Atmospheric greenhouse effect (W m ⁻²)	124	125	1.82
LW Cloud radiative forcing surface (W m ⁻²)	31.67	31.1	-0.54
SW clear sky surface (W m ⁻²)			2.61
SW clear sky top (W m ⁻²)			2.8
LW Cloud radiative forcing top (W m ⁻²)	-50.77	-50.4	0.36

1070 **Table 2** Global averages of heat fluxes and albedos. Atmospheric green house effect is computed as $\sigma T_s^4 - LW_{top}$, where σ is Stefan’s constant, T_s is the surface temperature and LW_{top} the net long wave flux at top of atmosphere.

Temperature (C/millennium)	Salinity (PSU/millennium)
----------------------------	---------------------------

	Global	Atlantic	Pa- cific	Indian	Global	Atlan- tic	Pa- cific	Indian
CTRL	0.6	0.7	0.5	0.6	0.05	0.05	0.04	0.09
HiRes	0.07	0.2	0.2	0.1	0.07	0.1	0.05	0.07

1075

Table 3 Drift of temperature and salinity in the deep ocean, averaged between 1000 m and bottom, for global ocean and Atlantic, Pacific and Indian basins. The drift is computed from basin averages from year 401 to 500, the period being used for all analyses.

Variable	CTRL	HiRes	Data	Data source	See
Air temperature (°C)	-21.47	-20.46	-19.41	NCEP/NCAR (Kalnay et al. 1996)	Fig. 4
Ocean temperature (°C)	3.90	3.87	3.86	PHC (Steele et al. 2001)	Fig. 4
Ocean Salinity (PSU)	34.69	34.65	34.72	PHC (Steele et al. 2001)	Fig. 4
SST (°C)	17.35	17.98	18.29	Reynolds (1988)	Fig. 8
Sea surface salinity	34.50	34.35	34.64	PHC (Steele et al. 2001)	Fig. 8
Precipitation, January (mm day ⁻¹)	2.56	2.69	2.54	CMAP (Xie and Arkin 1997)	Fig. 9
Precipitation, July (mm day ⁻¹)	2.64	2.74	2.71	CMAP (Xie and Arkin 1997)	Fig. 9
500 hPa height, filtered standard deviation (hPa)	24.6	26.7	26.4	NCEP/NCAR (Kalnay et al. 1996)	Fig. 10
Sea ice, NH, March (10 ⁶ km ²)	13.9	12.3	12.9	Gloersen and Campbell (1991)	Fig. 14
Sea ice, NH, Sept (10 ⁶ km ²)	5.8	4.2	6.2	Gloersen and Campbell (1991)	Fig. 14
Sea ice, NH, March (10 ⁶ km ²)	6.0	7.0	13.1	Gloersen and Campbell (1991)	Fig. 14
Sea ice, NH, Sept (10 ⁶ km ²)	15.4	15.1	20.1	Gloersen and Campbell (1991)	Fig. 14
SST, 2°S-2°N, (°C)	27.7	28.3	26.8	HadISST1 (1948-1999, Rayner et al. 2003)	Fig. 17
Zonal wind stress, 2°S-2°N (Pa)	-0.016	-0.017	-0.019	ERA40 (1948-2004, Uppala et al. 2005)	Fig. 17

1080

Table 4 Global averages of key climatic variables, synthesizing the information provided in the figure listed in the rightmost column.

	CTRL	HiRes	ERA40
Runoff (10 ³ m ³ s ⁻¹)	-221.8	-196.8	-200.1
P-E (10 ³ m ³ s ⁻¹)	-232.1	-246.7	-134.0
Sea ice (10 ³ m ³ s ⁻¹)	-6.2	-6.7	<i>n.a.</i>
Total (10 ³ m ³ s ⁻¹)	-460.1	-450.2	-334.1

1085

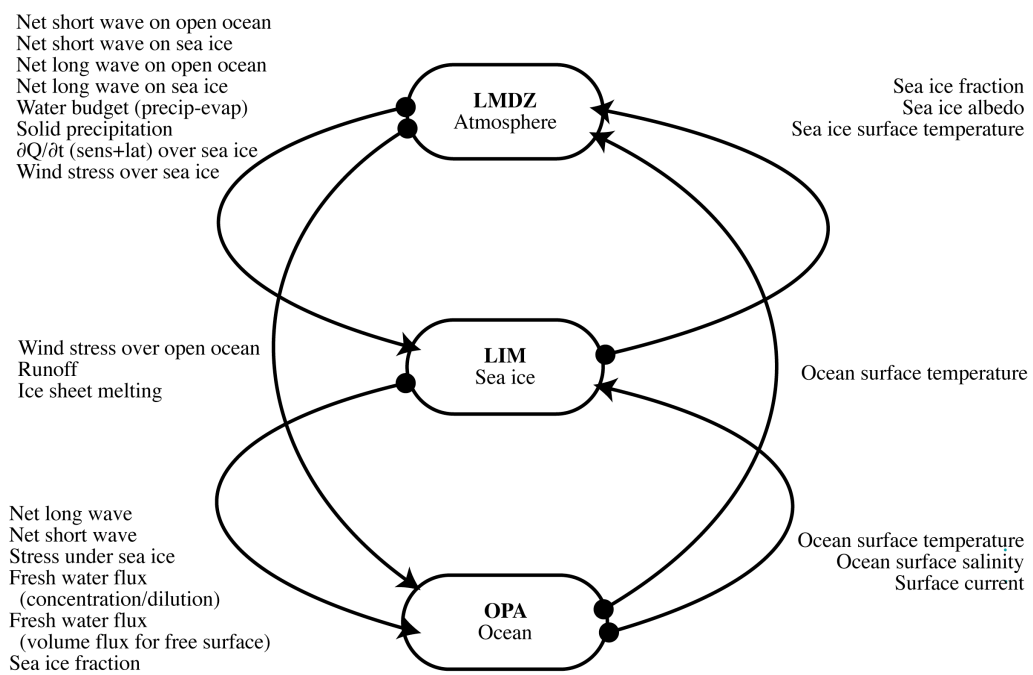
Table 5 Comparison of the fresh water budget (in mSv \equiv 10³ m³s⁻¹) of different simulations with climatology of continental runoff discharge from UNESCO and evaporation minus evaporation (E-P) from ERA40 (Uppala et al. 2005), north of 40°N in the Atlantic and Arctic Ocean.

1085 **13 List of figures**

- Fig. 1** Fields exchanged between ocean, sea ice and atmosphere models. 28
- Fig. 2** Evolution of global and annual averages of a) net surface heat flux (W m^{-2}),
b) temperature at 2 m (C), c) snow mass (kg m^{-2}). D) ice volume (10^{12} m^3) for Southern
hemisphere (SH) and Northern hemisphere. Red for CTRL and green for HiRes..... 29
- 1090 **Fig. 3** Difference between HiRes and CTRL in latitudinal distribution (annual mean) of a)
heat flux at TOA (black: short wave, red: long wave, green: net), b) heat flux at the
surface (black: short wave, red: long wave, green: sensible, blue: latent), c) planetary
(black) and surface (red) albedos, d) air temperature at 2 m. 30
- Fig. 4** Zonal and annual means. a) CTRL minus PHC (Steele et al. 2001) climatology for the
1095 ocean temperature, NCEP/NCAR (Kalnay et al. 1996) for the atmosphere temperature. b)
Temperature differences between HiRes and CTRL. c) CTRL minus PHC climatology
(Steele et al. 2001) for the ocean salinity. d) Salinity differences between HiRes and
CTRL. See **Table 4** for global averages and **Fig. 5** for statistics. PHC climatology merges
the 1998 version of the World Ocean Atlas with the regional Arctic Ocean Atlas (Steele
1100 et al. 2001). 31
- Fig. 5** These Taylor diagrams (Taylor 2001) summarize the standard deviation and the
correlation coefficient between model and data. The correlation R is computed between
model and data. It is given on the plot by the azimuthal position (i.e. then angle between
1105 the abscissa and the line that joints origin to data point is $\cos^{-1}(R)$). The standard
deviation between model and data E' is normalized by the standard deviation of data and
the result is plotted as the radial distance to the graphic origin. A high value of the
correlation (resp. a low value of the angle) means that the model pattern is close to the
data pattern. A normalized standard deviation close to 1 means that the amplitude of the
1110 pattern are close in model and data. The centred RMS between model and data is the
linear distance between the observations (always on the abscissa, at radius 1) and the
model points. It is a measure of the 'distance' between model and data. CTRL is in red,
HiRes in green. Fields are listed in the figure, with the indication of the symbol used, the
units of the standard deviation, and the figure to which it refers. Left panel is for
1115 atmospheric variables and right for ocean and sea ice. The data used are detailed in each
corresponding figures captions, and in **Table 4**. For sea ice, the correlation is computed
only where sea ice is present either in observation, in CTRL or in HiRes..... 32
- Fig. 6** Annual mean heat transports, for CTRL (red) and HiRes (green). a) total transport
(ocean plus atmosphere). The black line is the transport implied by the net radiative flux
1120 at top of atmosphere (TOA) from ERBE data (Barkstrom 1984). To obtain the transport,
the TOA net flux is integrated from the South Pole, and arbitrarily set to zero at the
equator. Wunsch (2005) estimated the error to $\pm 1.1 \cdot 10^{15} \text{ W}$ at the latitudes of the
extrema. b) Atmospheric heat transport. Estimates from NCEP/NCAR (Kalnay et al.
1996, black line) and ERA40 reanalysis (Uppala et al. 2005) have been added. c) ocean
heat transport. Estimates from Trenberth and Caron (2001) has been added (black line). d)
1125 Differences between model and observations. e) Atlantic heat transport. Estimates and
error bars from Ganachaud and Wunsch (2000) has been added. 33
- Fig. 7** Stream function of the Atlantic meridional overturning. Left: CTRL, right: HiRes.
Isoline every 2 Sv, and every 10 Sv above 20 Sv..... 34
- Fig. 8** a) difference between CTRL simulated sea surface temperature (annual mean) and the
1130 climatology of Reynolds (1988). Isolines are plotted every 1°C . b) difference between
HiRes and CTRL SST. Isolines are plotted every 0.5°C . c) difference between CTRL
simulated sea surface salinity (annual mean) and the PHC (Steele et al. 2001)

	climatology. Isolines are plotted every 0.5 PSU. d) Salinity differences between HiRes and CTRL. Isolines are plotted every 0.25 PSU. See Table 4 for global averages and Fig. 5 for statistics. 35
1135	Fig. 9 January (left) and July (right) precipitation (in mm day ⁻¹) for CMAP (Xie and Arkin 1997) data (top), CTRL (middle) and HiRes (bottom). See Table 4 for global averages and Fig. 5 for statistics. 36
1140	Fig. 10 High-pass filtered standard deviation of the 500 hPa geopotential height for DJF (units: hPa). Top: NCEP/NCAR Reanalyses (1980-1999, Kalnay et al. 1996), middle: CTRL, bottom: HiRes. See Table 4 for global averages and Fig. 5 for statistics. 37
	Fig. 11 First (top) and second (bottom) empirical orthogonal functions (EOF) computed by a principal component analysis of the sea-level pressure. Left: NCEP/NCAR (Kalnay et al. 1996) reanalyses, middle: CTRL, right: HiRes. 38
1145	Fig. 12 Correlations between observed and simulated EOF of SLP. See text for details. 38
	Fig. 13 Maximum depth of the mixed layer in meter. Isolines every 250 m. The thick red lines show the winter and summer position of the sea ice edge (limit of 15% of sea ice concentration). a) Data from Montegut et al. (2004) for the mixed layer and Gloersen and Campbel (1991) for the ice edge, b) Difference between HiRes and CTRL. Full colors correspond to the 99% Student test significant differences. c) CTRL, d) HiRes. 39
1150	Fig. 14 Winter sea ice thickness for the model (top), and winter and summer ice edges (bottom) for model and data (Gloersen and Campbell 1991). See Table 4 for global averages and Fig. 5 for statistics. 40
	Fig. 15 Salt transport (10 ⁶ kg s ⁻¹) by the gyre component for CTRL (red) and HiRes (green). See appendix 9.2 for the computation of the gyre component. 40
1155	Fig. 16 Left panel: barotropic stream function in Sv in the Southern Hemisphere for CTRL (red) and HiRes (green). Right panel : zonal average of the zonal wind stress for CTRL (red), HiRes (green) and ERA 40 (black) (Uppala et al. 2005). 41
1160	Fig. 17 Mean seasonal cycle of the SST (left panel) and zonal wind stress (right panel), with annual mean removed and averaged between 2°S and 2°N. Isoline every 0.5°C and 0.01 Pa. Bottom plots display the annual average of models and data averaged between 2°S and 2°N. Data are from HadISST1 (1948-1999, Rayner et al. 2003) for SST and from ERA40 (1948-2004, Uppala et al. 2005) for wind stress. See Table 4 for global averages and Fig. 5 for global statistics. 42
1165	Fig. 18 Monthly standard deviation of SST and zonal wind stress for observations a] HadISST (Rayner et al. 2003), d] ERA40 (Uppala et al. 2005), b,e] CTRL 100 years c, f], HiRes 100 years. g] Zonal mean of wind stress standard deviation between 180 W and 140 W (black: ERA40, red: CTRL, green: HiRes). h, i] Interannual coupling strength for CTRL (h), linear fit = 4.3 10 ⁻³ N m ⁻² K ⁻¹) and HiRes (i), linear fit = 6.0 10 ⁻³ N m ⁻² K ⁻¹), measured as the slope of monthly <i>anomaly of Tau_{Niño4} = f(anomaly of SST_{Niño3})</i> . Contours are 0.2 C for a]-c] and 0.05 N m ⁻² for d]-f]. 43
1170	

14 Figures



1175

Fig. 1 Fields exchanged between ocean, sea ice and atmosphere models.

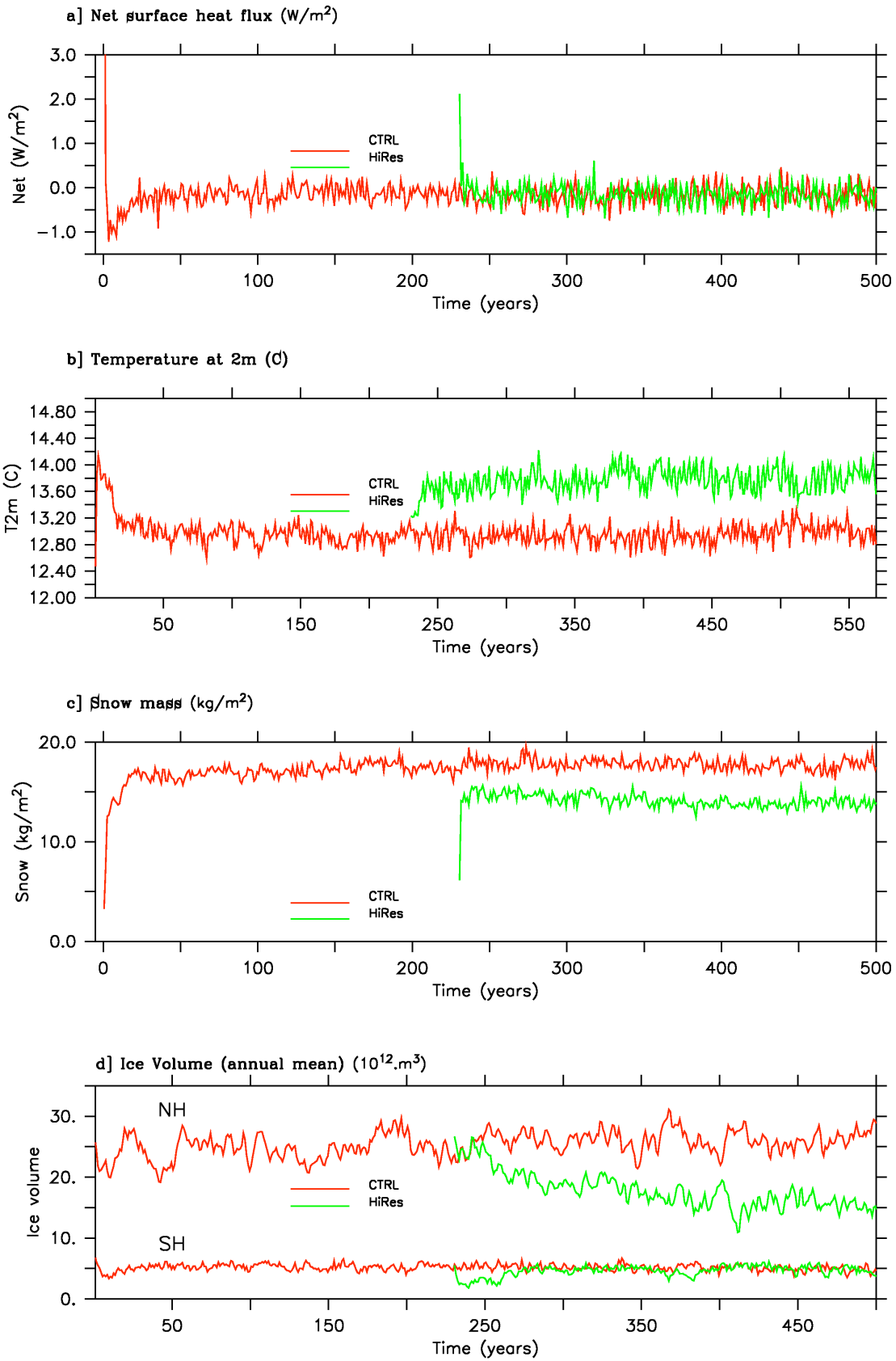


Fig. 2 Evolution of global and annual averages of a) net surface heat flux (W m⁻²), b) temperature at 2 m (C), c) snow mass (kg m⁻²). D) ice volume (10¹² m³) for Southern hemisphere (SH) and Northern hemisphere. Red for CTRL and green for HiRes

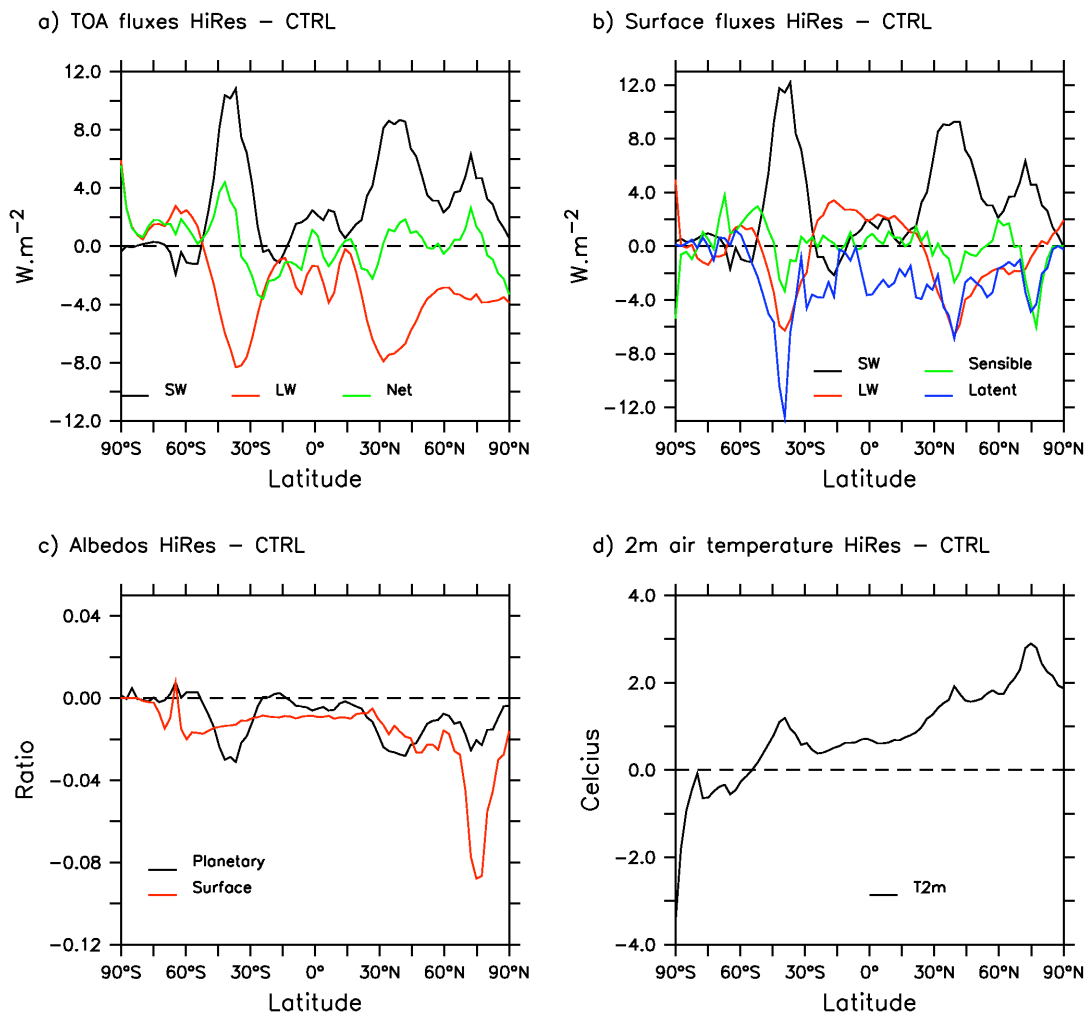


Fig. 3 Difference between HiRes and CTRL in latitudinal distribution (annual mean) of a) heat flux at TOA (black: short wave, red: long wave, green: net), b) heat flux at the surface (black: short wave, red: long wave, green: sensible, blue: latent), c) planetary (black) and surface (red) albedos, d) air temperature at 2 m.

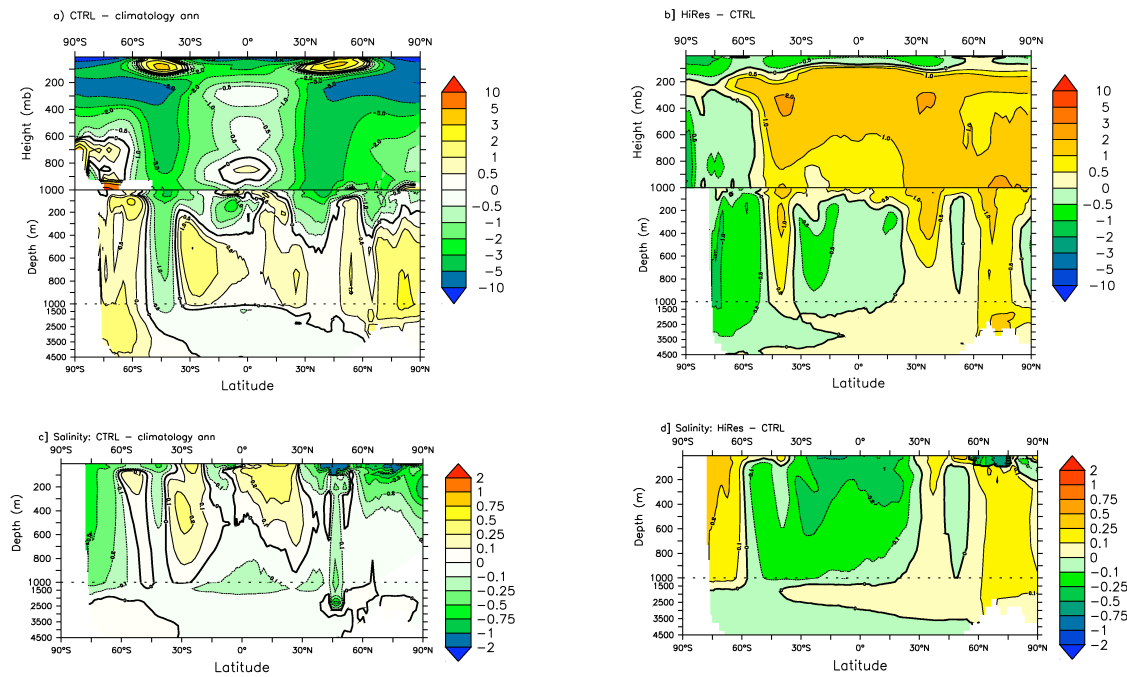
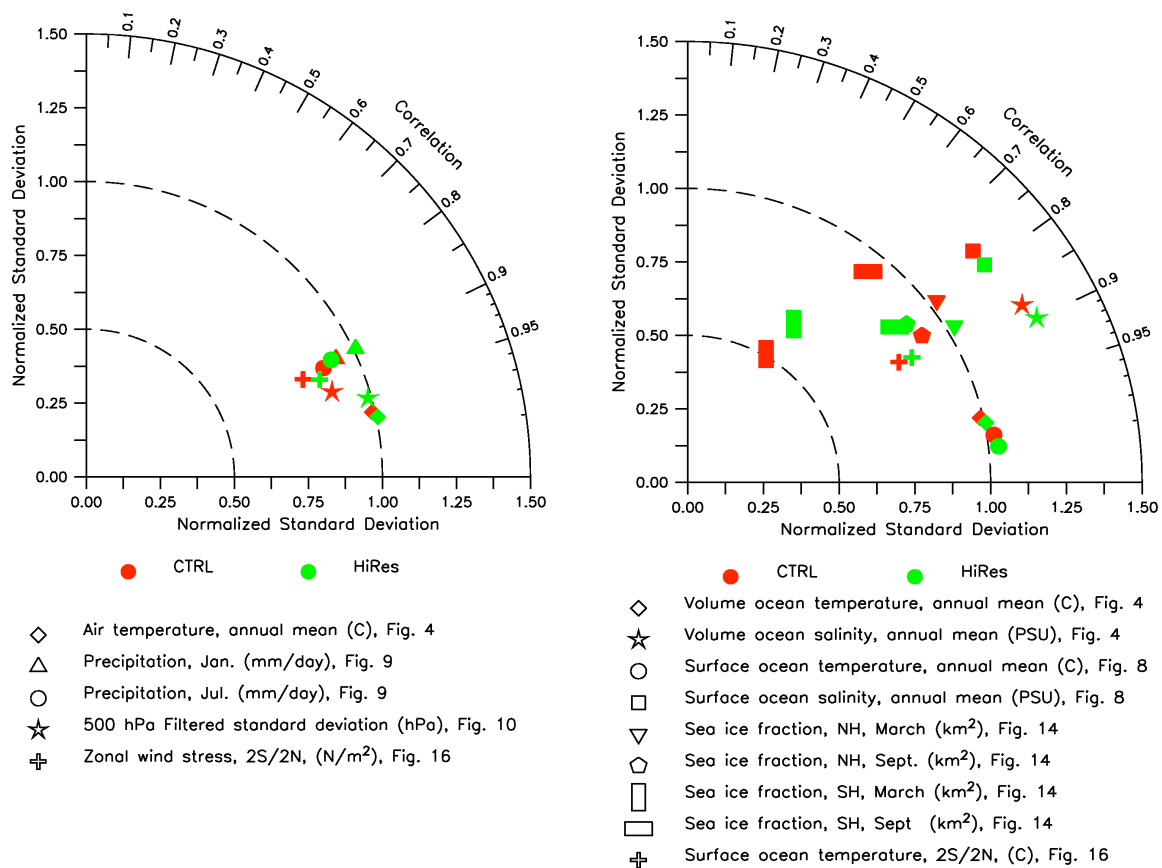
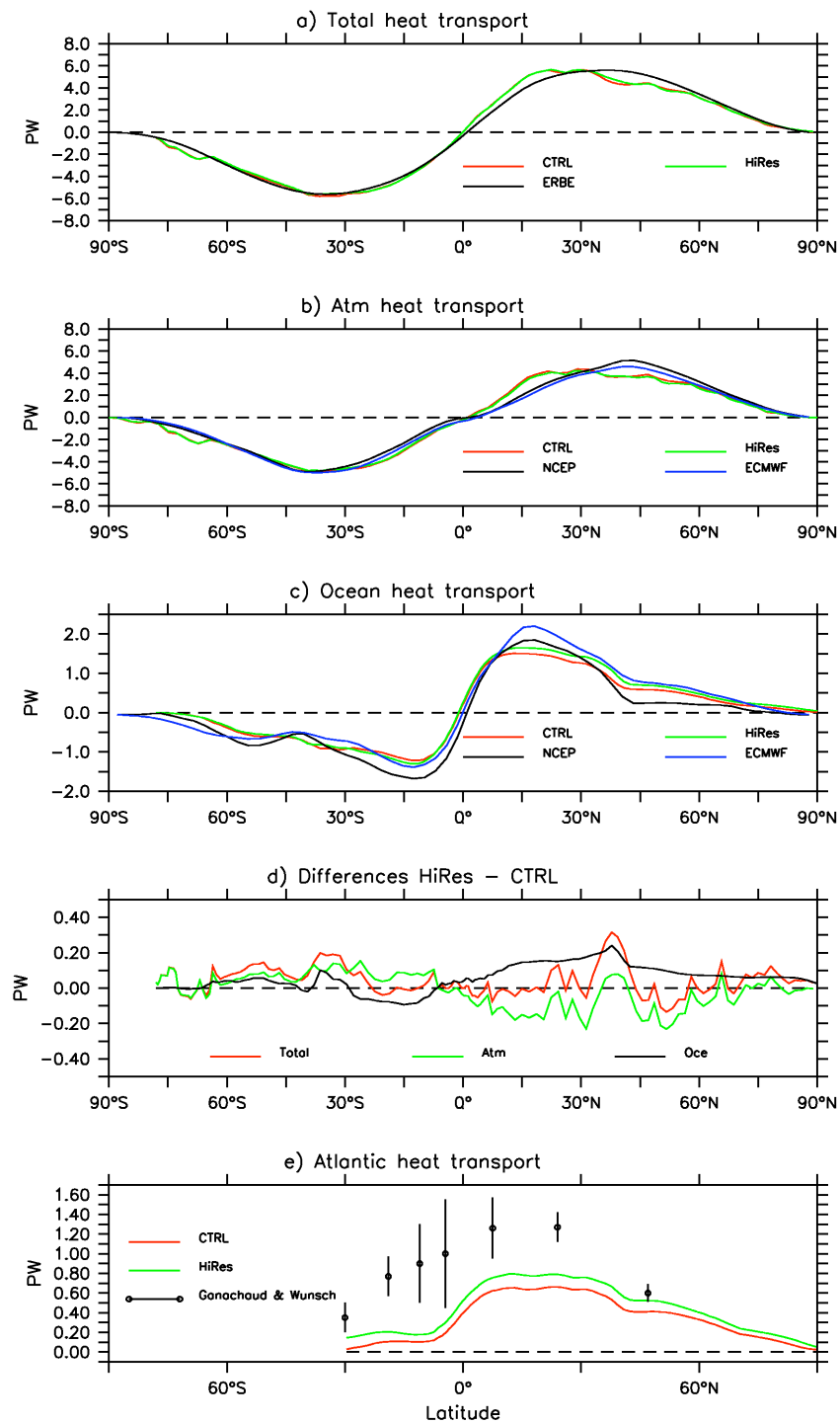


Fig. 4 Zonal and annual means. a) CTRL minus PHC (Steele et al. 2001) climatology for the ocean temperature, NCEP/NCAR (Kalnay et al. 1996) for the atmosphere temperature. b) Temperature differences between HiRes and CTRL. c) CTRL minus PHC climatology (Steele et al. 2001) for the ocean salinity. d) Salinity differences between HiRes and CTRL. See **Table 4** for global averages and **Fig. 5** for statistics. PHC climatology merges the 1998 version of the World Ocean Atlas with the regional Arctic Ocean Atlas (Steele et al. 2001).



1195 **Fig. 5** These Taylor diagrams (Taylor 2001) summarize the standard deviation and the correlation coefficient between model and data. The correlation R is computed between model and data. It is given
 1200 on the plot by the azimuthal position (i.e. then angle between the abscissa and the line that joints origin to data point is $\cos^{-1}(R)$). The standard deviation between model and data E' is normalized by the
 standard deviation of data and the result is plotted as the radial distance to the graphic origin. A high
 1205 value of the correlation (resp. a low value of the angle) means that the model pattern is close to the
 data pattern. A normalized standard deviation close to 1 means that the amplitude of the pattern are
 close in model and data. The centred RMS between model and data is the linear distance between the
 observations (always on the abscissa, at radius 1) and the model points. It is a measure of the 'distance'
 between model and data. CTRL is in red, HiRes in green. Fields are listed in the figure, with the
 indication of the symbol used, the units of the standard deviation, and the figure to which it refers. Left
 panel is for atmospheric variables and right for ocean and sea ice. The data used are detailed in each
 corresponding figures captions, and in **Table 4**. For sea ice, the correlation is computed only where
 sea ice is present either in observation, in CTRL or in HiRes.



1210

Fig. 6 Annual mean heat transports, for CTRL (red) and HiRes (green). a) total transport (ocean plus atmosphere). The black line is the transport implied by the net radiative flux at top of atmosphere (TOA) from ERBE data (Barkstrom 1984). To obtain the transport, the TOA net flux is integrated from the South Pole, and arbitrarily set to zero at the equator. Wunsch (2005) estimated the error to $\pm 1.1 \cdot 10^{15}$ W at the latitudes of the extrema. b) Atmospheric heat transport. Estimates from NCEP/NCAR (Kalnay et al. 1996, black line) and ERA40 reanalysis (Uppala et al. 2005) have been added. c) oceanic heat transport. Estimates from Trenberth and Caron (2001) has been added (black line). d) Differences between model and observations. e) Atlantic heat transport. Estimates and error bars from Ganachaud and Wunsch (2000) has been added.

1215

1220

1220

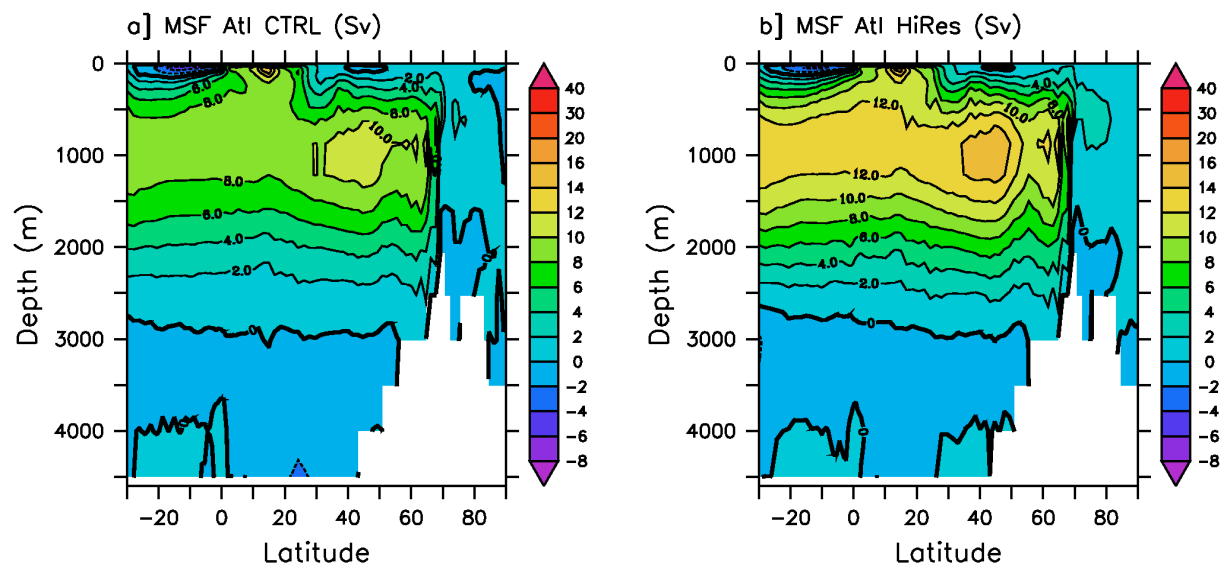
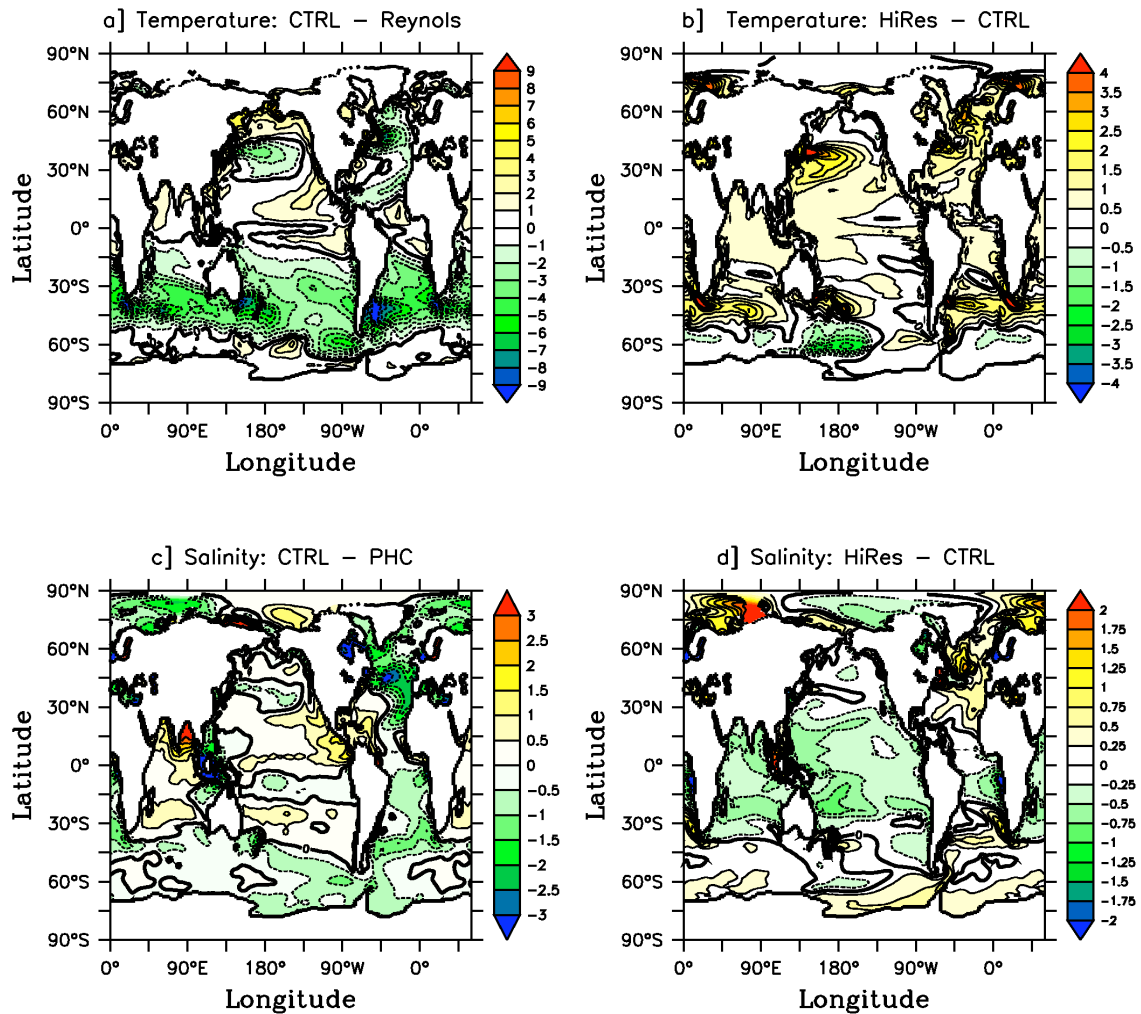


Fig. 7 Stream function of the Atlantic meridional overturning. Left: CTRL, right: HiRes. Isoline every 2 Sv, and every 10 Sv above 20 Sv.



1225 **Fig. 8** a) difference between CTRL simulated sea surface temperature (annual mean) and the climatol-
 1230 ogy of Reynolds (1988). Isolines are plotted every 1°C. b) difference between HiRes and CTRL SST. Isolines are plotted every 0.5°C. c) difference between CTRL simulated sea surface salinity (annual mean) and the PHC (Steele et al. 2001) climatology. Isolines are plotted every 0.5 PSU. d) Salinity differences between HiRes and CTRL. Isolines are plotted every 0.25 PSU. See **Table 4** for global averages and **Fig. 5** for statistics.

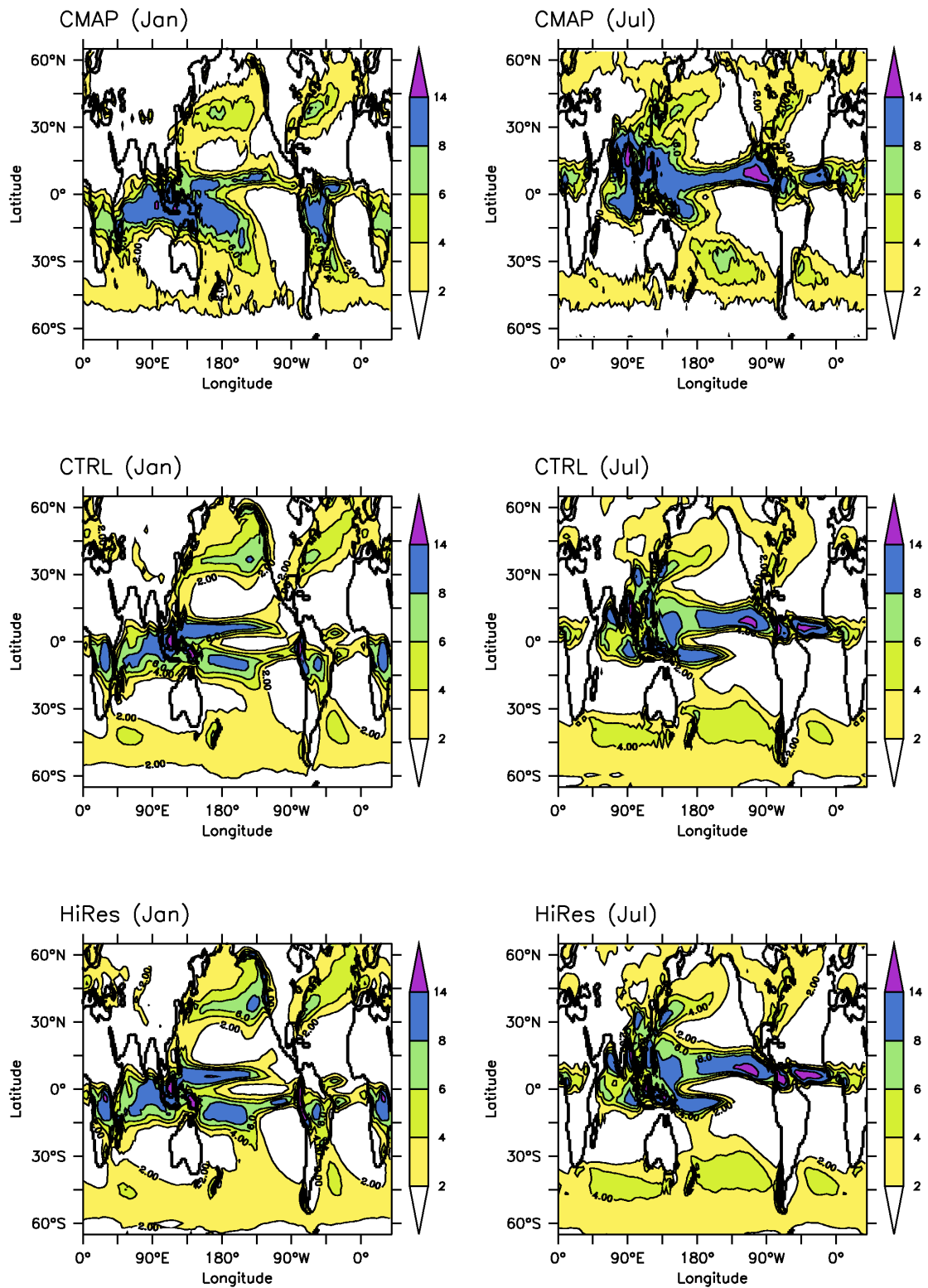
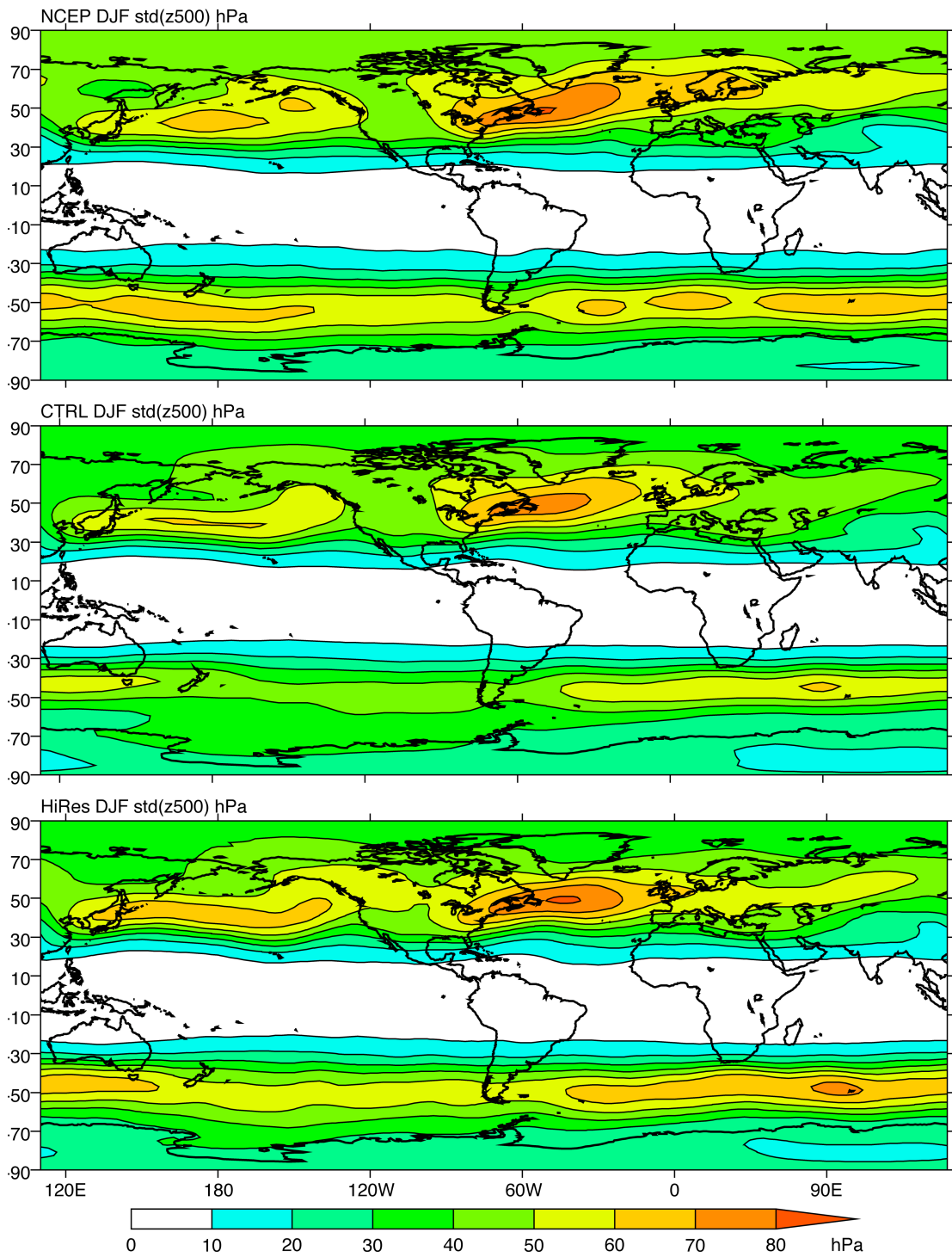
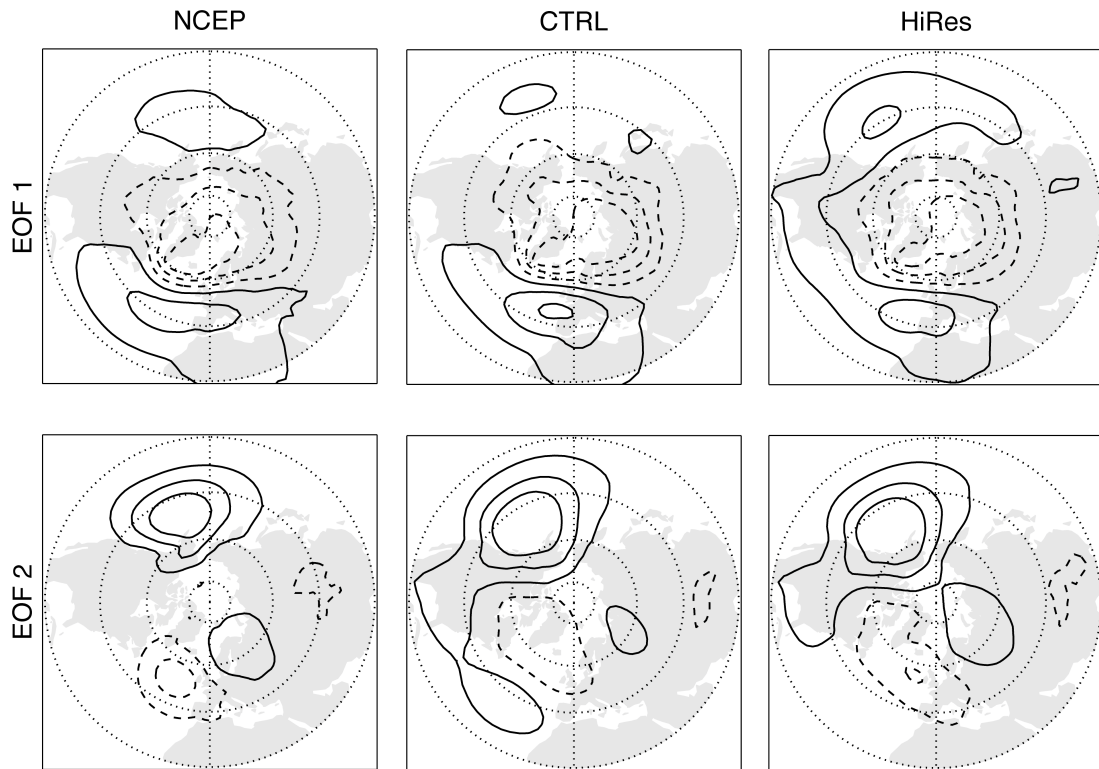


Fig. 9 January (left) and July (right) precipitation (in mm day⁻¹) for CMAP (Xie and Arkin 1997) data (top), CTRL (middle) and HiRes (bottom). See **Table 4** for global averages and **Fig. 5** for statistics.



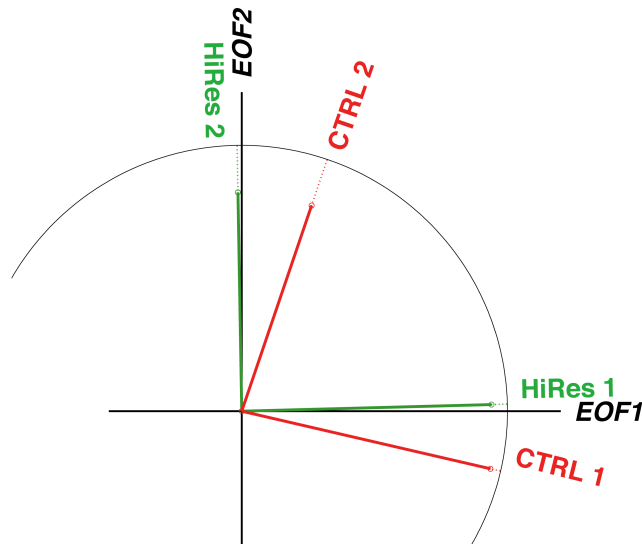
1235

Fig. 10 High-pass filtered standard deviation of the 500 hPa geopotential height for DJF (units: hPa). Top: NCEP/NCAR Reanalyses (1980-1999, Kalnay et al. 1996), middle: CTRL, bottom: HiRes. See **Table 4** for global averages and **Fig. 5** for statistics.



1240

Fig. 11 First (top) and second (bottom) empirical orthogonal functions (EOF) computed by a principal component analysis of the sea-level pressure. Left: NCEP/NCAR (Kalnay et al. 1996) reanalyses, middle: CTRL, right: HiRes.



1245

Fig. 12 Correlations between observed and simulated EOF of SLP. See text for details.

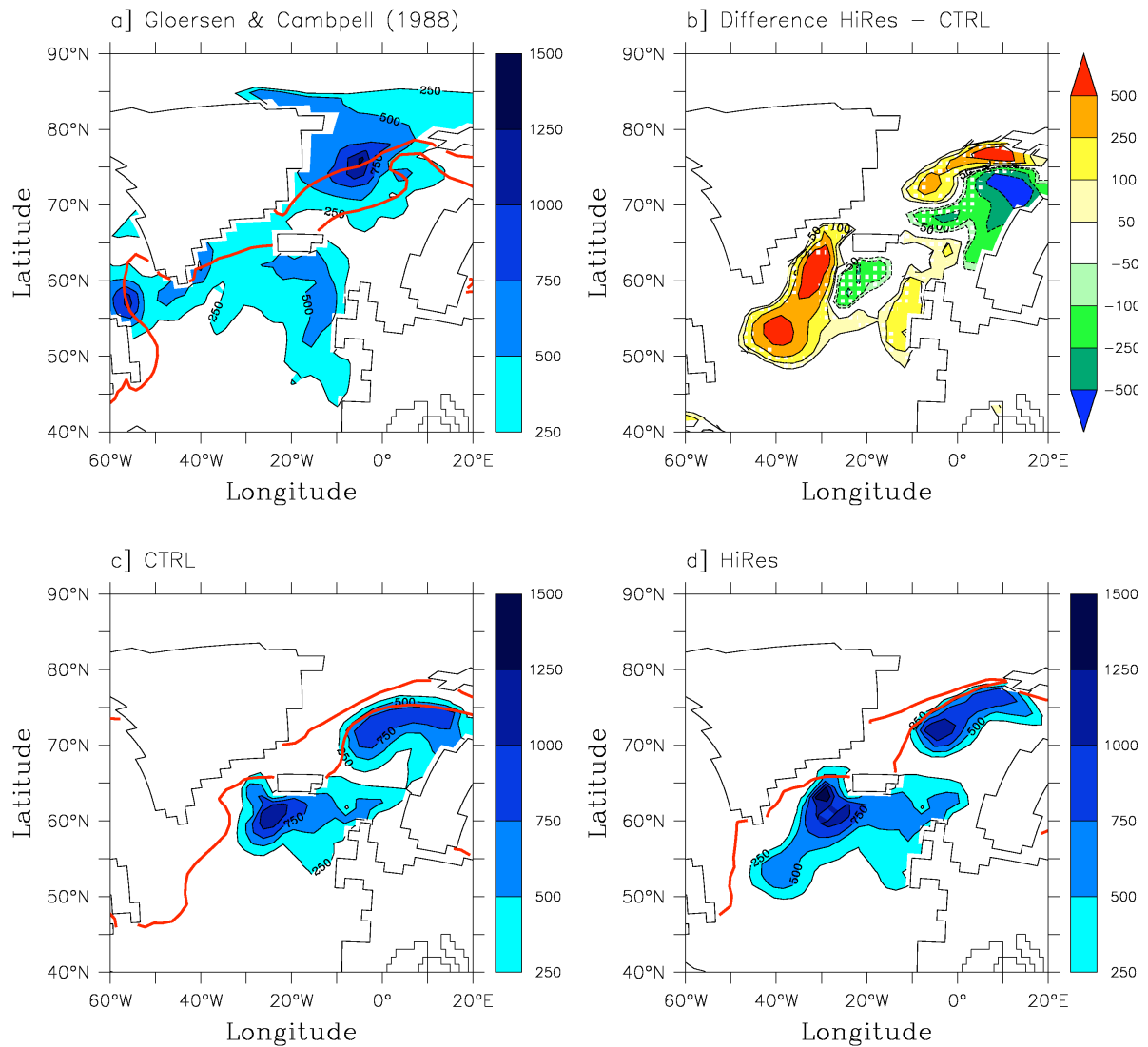
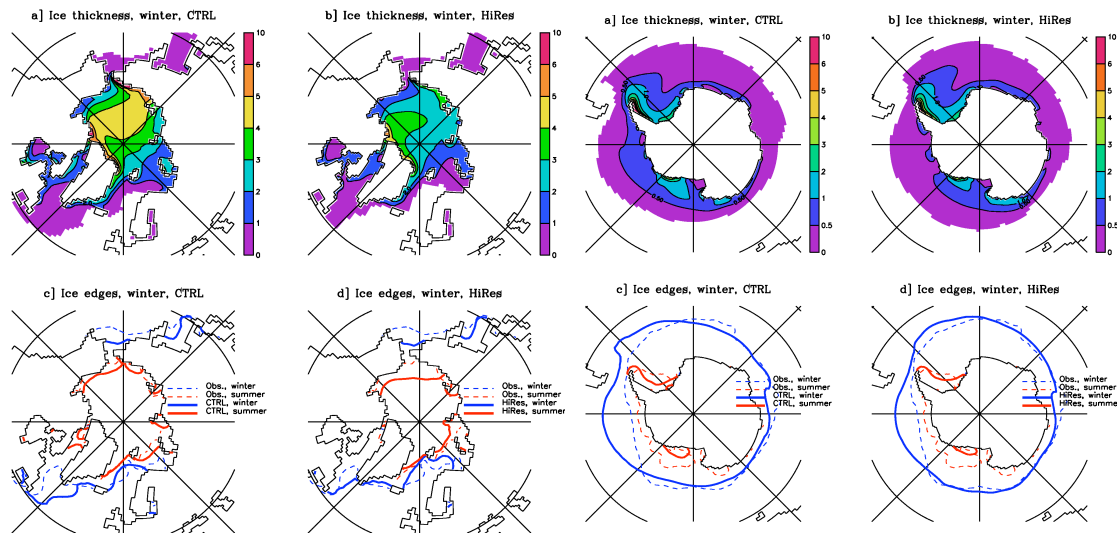


Fig. 13 Maximum depth of the mixed layer in meter. Isolines every 250 m. The thick red lines show the winter and summer position of the sea ice edge (limit of 15% of sea ice concentration). a) Data from Montegut et al. (2004) for the mixed layer and Gloersen and Campbel (1991) for the ice edge, b) Difference between HiRes and CTRL. Full colors correspond to the 99% Student test significant differences. c) CTRL, d) HiRes.



1255 **Fig. 14** Winter sea ice thickness for the model (top), and winter and summer ice edges (bottom) for model and data (Gloersen and Campbell 1991). See **Table 4** for global averages and **Fig. 5** for statistics.

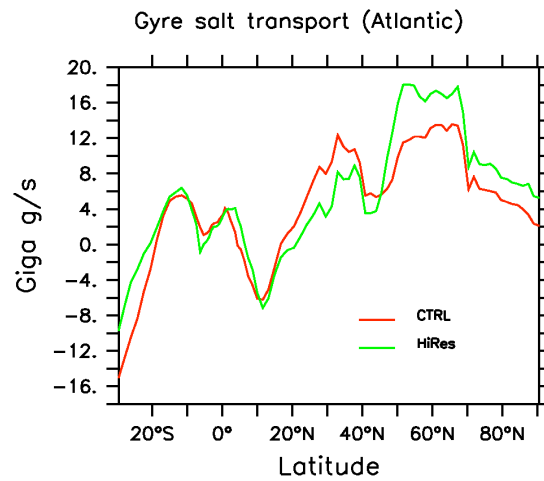
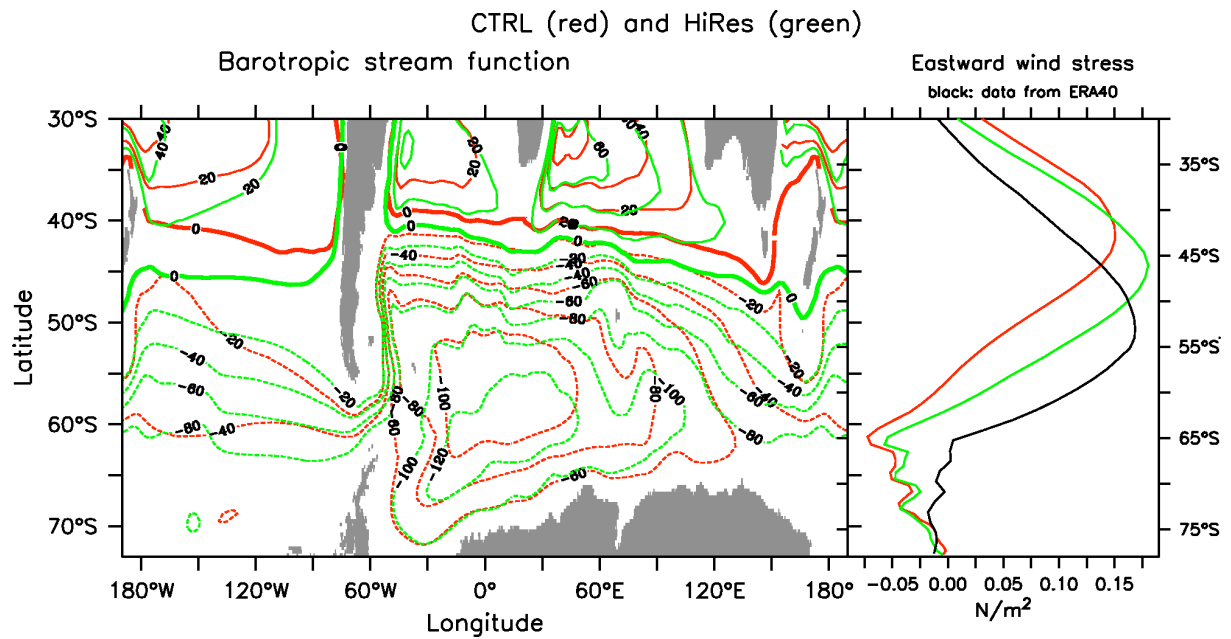
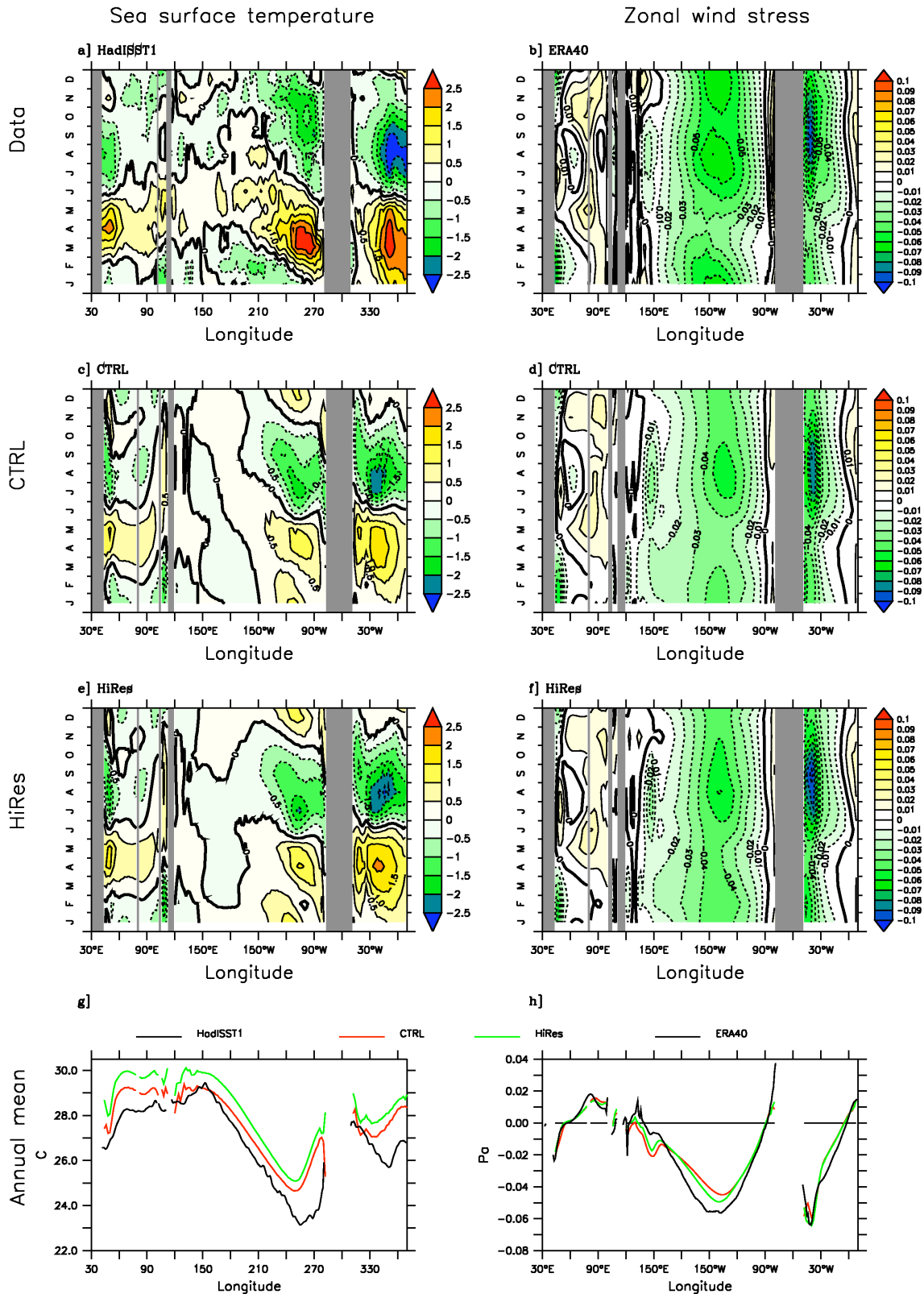


Fig. 15 Salt transport (10^6 kg s^{-1}) by the gyre component for CTRL (red) and HiRes (green). See appendix 9.2 for the computation of the gyre component.

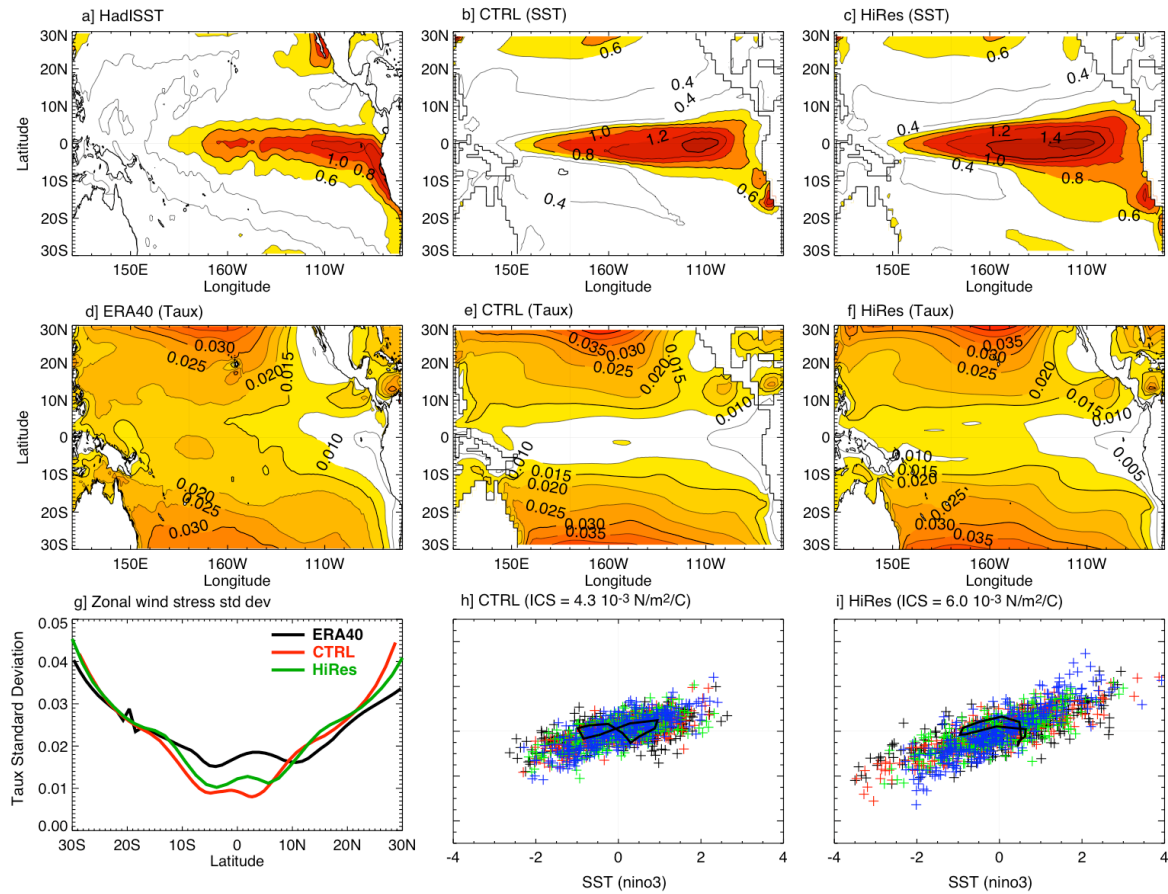


1260

Fig. 16 Left panel: barotropic stream function in Sv in the Southern Hemisphere for CTRL (red) and HiRes (green). Right panel : zonal average of the zonal wind stress for CTRL (red), HiRes (green) and ERA 40 (black) (Uppala et al. 2005).



1265 **Fig. 17** Mean seasonal cycle of the SST (left panel) and zonal wind stress (right panel), with annual
 1270 mean removed and averaged between 2°S and 2°N. Isoline every 0.5°C and 0.01 Pa. Bottom plots dis-
 play the annual average of models and data averaged between 2°S and 2°N. Data are from HadISST1
 (1948-1999, Rayner et al. 2003) for SST and from ERA40 (1948-2004, Uppala et al. 2005) for wind
 stress. See Table 4 for global averages and Fig. 5 for global statistics.



1270

Fig. 18 Monthly standard deviation of SST and zonal wind stress for observations a) HadISST (Rayner et al. 2003), d) ERA40 (Uppala et al. 2005), b,e) CTRL 100 years c, f), HiRes 100 years. g) Zonal mean of wind stress standard deviation between 180 W and 140 W (black: ERA40, red: CTRL, green: HiRes). h, i) Interannual coupling strength for CTRL (h), linear fit = $4.3 \cdot 10^{-3} \text{ N m}^{-2} \text{ K}^{-1}$ and HiRes (i), linear fit = $6.0 \cdot 10^{-3} \text{ N m}^{-2} \text{ K}^{-1}$, measured as the slope of monthly *anomaly of* $Tau_{Ni\tilde{4}} = f(\text{anomaly of } SST_{Ni\tilde{3}})$. Contours are 0.2 C for a]-c) and 0.05 N m^{-2} for d]-f).

1275

1

1280